Studies for the PIENU Experiment and on the Direct Radiative Capture of Muons in Zirconium

by

Dorothea vom Bruch

A THESIS SUBMITTED IN PARTIAL FULFILLMENT
OF THE REQUIREMENTS FOR THE DEGREE OF

Master of Science

in

THE FACULTY OF GRADUATE AND POSTDOCTORAL STUDIES
(Physics)

The University Of British Columbia
(Vancouver)

December 2013

Abstract

The branching ratio of pions decaying to positrons and muons $R = \frac{\pi^+ \to e^+ \nu_e + \pi^+ \to e^+ \nu_e \gamma}{\pi^+ \to \mu^+ \nu_\mu + \pi^+ \to \mu^+ \nu_\mu \gamma}$ has been calculated with very high precision in the Standard Model of particle physics. So far, the theoretical value of $R = 1.2352(1) \cdot 10^{-4}$ is 40 times more precise than the current experimental value of $R = 1.230(4) \cdot 10^{-4}$. To test this variable with respect to deviations from the Standard Model, the experimental precision needs to be improved, which is why the PIENU experiment aims at a precision of less than 10^{-3}, i.e. an improvement of an order of magnitude over the current precision. At this level, mass scales $\sim 1000\,\mathrm{TeV/c^2}$ can be probed for evidence of new pseudo-scalar interactions. The data collected with the experimental setup also allows for a search of sterile neutrinos. When determining the branching ratio, various systematic corrections are applied. The largest among these is due to electro-magnetic shower leakage out of the calorimeters and radiative decays. It was calculated to be $(2.25 \pm 0.06)\,\%$ in this thesis.

In the second part of the thesis, an experiment on the direct radiative capture of muons in zirconium is described. One theoretical extension to the Standard Model involves a new light and weakly interacting particle in the muon sector which does not conserve parity. This can be studied experimentally with polarized muons that undergo the direct radiative capture into the 2S state of a medium mass target nucleus. During this capture, longitudinal muon polarization is conserved and the muons instantly undergo the 2S-1S transition emitting a second photon. Studying the angular distribution of this second photon indicates whether or not the process is parity violating, which would manifest physics beyond the Standard Model. The direct radiative capture of a muon into an atom in the 1S or 2S state has not been observed yet. Therefore, data was taken in 2012 to study the radiative

capture of muons in zirconium. The analysis method of this data set is described with a blind analysis technique.

Preface

In February 2012, I joined the PIENU collaboration, which has about 25 members from 11 institutions. I actively participated in the run period between May and December 2012 by taking shifts in the experiment control room. In terms of data analysis, I focused on determining a lower limit on the systematic correction to the branching ratio that accounts for energy leakage out of the calorimeters and radiative decays. The basic procedure was established by Chloé Malbrunot and is described in her doctoral thesis [1]. I improved the method by optimizing the cuts that were applied (indicated in the main text), and by adding a new correction to account for radiative decays. Tristan Sullivan determined a second estimate for the correction [2] and I implemented a procedure to combine the two estimates.

In November 2012, an experiment to study the direct radiative capture of negative muons into zirconium was proposed. I assessed the feasibility of this experiment with the PIENU detector and the M13 beamline at TRIUMF. After concluding that it was realistic, I proposed an experimental run which was realized during four days in December 2012. I established the procedure for analyzing this data set employing a blind analysis method. By implementing a new fitting procedure for the waveform of the calorimeter, I improved its time resolution by a factor of four. I also used this fit for pulse shape discrimination and was able to identify neutrons and photons within the calorimeter. These new tools allowed me to decide on cuts to select the signal process of the direct muon capture and suppress backgrounds. Anthony Fradette and Maxim Pospelov provided the necessary theoretical calculations to characterize the signal events which I used to simulate the signal process in a GEANT4 simulation. Based on this simulation, I estimated the significance of the signal with respect to the background events in the data and developed different

procedures to extract the signal from the background.

Table of Contents

List of Tables

List of Figures

Glossary

ADC Analog to Digital Converter.

ARC Atomic Radiative Capture.

B1 and B2 Two plastic scintillator counters in front of the target of the PIENU experiment.

CsI Cesium Iodide.

DAQ Data Acquisition System.

FADC Flash Analog to Digital Converter.

GEANT4 GEometry ANd Tracking: Toolkit which uses Monte Carlo Methods to simulate the passage of particles through matter, written in C++..

M13 Pion beam line in the meson hall at TRIUMF.

MC Monte Carlo.

MDAR Muon Decays At Rest.

MDIF Muon Decays In Flight.

NaI Sodium Iodide.

NDF Number of Degrees of Freedom.

NP New Physics.

PDAR Pion Decays At Rest.

PDIF Pion Decays In Flight.

PMT Photo Multiplier Tube.

RF Radio Frequency.

SM Standard Model.

T1 and T2 Two plastic scintillator counters before and after the third wire chamber of the PIENU experiment.

Tg Target.

TOF Time Of Flight.

TRIUMF Canada's National Laboratory for Particle and Nuclear Physics.

WC Wire Chamber.

Acknowledgments

In the first place, I want to thank my supervisor Doug Bryman for his support and advice, and especially for making the muon capture experiment possible, and for guiding me throughout the experimental procedure as well as the data analysis.

Furthermore, I am very grateful for discussions with Toshio Numao on the lower limit, for the explanations and help provided by Alexey Sher, Luca Doria, and Dima Vavilov, and for the collaboration with the PhD students Tristan Sullivan, Shintaro Ito and Saul Cuen-Rochin. Special thanks goes to Luca Doria for his quick and efficient proof-reading of this thesis. In particular, I want to acknowledge the insightful explanations and discussions with Richard Mischke during my very first shifts and his comments on my analysis as well as the proof-reading of this thesis.

A word of thanks is due to Maxim Pospelov and Anthony Fradette from the University of Victoria for their contributions to the theoretical predictions for the muon capture experiment, and their inspiring comments and clear explanations.

Finally, I would like to thank Tegan Macdonald for the proof-reading of the thesis from an outside perspective, and for the many lunch breaks with the TITAN group.

Chapter 1

Introduction

1.1 Outline of the Thesis

This thesis describes work performed on the data analysis of the PIENU experiment as well as a muon capture experiment which was conducted using the same detector. After motivating both experiments in Chapter 1 the setup of the PIENU experiment is described in Chapter 2. Chapter 3 deals with the procedure for data analysis with special focus on systematic effects. Finally, chapter Chapter 4 explains how the detector was modified to accommodate the muon capture experiment, describes the analysis technique and presents the preliminary results. Chapter 5 summarizes the results for both the PIENU experiment and the muon capture experiment, proposes further studies and outlines the impacts of the results.

1.2 Motivation for the PIENU Experiment

Research in particle physics is pursued at three different frontiers nowadays: at the high energy scale, in the cosmic sector, and with high precision and intensity experiments. The PIENU ($\pi \to e\nu$) experiment belongs to the last category; it aims to explore physics beyond the Standard Model (SM) by studying rare pion decays to positrons and muons. The measured branching ratio of pions decaying to positrons and to muons will be compared to the theoretically predicted value $R = 1.2352(1) \cdot 10^{-4}$ [3] which has been very precisely calculated within the SM.

So far, the theoretical value is 40 times more precise than the experimental value of $R = 1.230(4) \cdot 10^{-4}$ [4], which is why PIENU aspires at a level of relative precision of less than 10^{-3}, i.e. an improvement of an order of magnitude over the current precision.

Validating the SM with experimental results has been the task of elementary particle physicists for the past five decades. In particular, the discovery of a Higgs like particle last year at the Large Hadron Collider was a big success for the SM [5]. However, many questions and puzzles remain unsolved in the domain of particle physics. Firstly, the discovery of neutrino oscillations [6] requires neutrinos to be massive particles. Their hierarchy however, and the mechanism of how they obtain their mass are still unknown and not predicted within the current standard theory. In addition, the reason for the number of lepton families (electrons, muons, taus) remains a mystery, as well as the large range of mass scales among the elementary particles. Furthermore, observations of the rotation speed of galaxies [7], and other observations such as galactic clusters [8] and the cosmic microwave background [9], imply that normal matter cannot solely account for the behaviour of stars and gas circling around the center of a galaxy. Hence, a different explanation, such as the existence of dark matter, is needed to explain these phenomena. Elementary particles not included in the SM are possible candidates to explain dark matter.

Evidently, there is need for extensions or modifications to the existing SM in order to consistently explain the processes in our universe. At the level of precision that the PIENU experiment aims for, mass scales $\sim 1000\,\mathrm{TeV/c^2}$ can be probed for evidence of new pseudo-scalar interactions. In addition, the data collected with the experimental setup allows for a search of sterile neutrinos. These sterile neutrinos are a possible candidate for dark matter [10].

Thorough understanding of the experimental setup, background processes, and systematic effects is required in order to obtain the desired precision. The study of one of these systematic effects, due to the electro-magnetic shower leakage out of the calorimeters and radiative decays, is the main focus in this thesis concerning the PIENU experiment .

1.3 Motivation for the Muon Capture Experiment

In the search for physics beyond the SM the experiments at the Large Hadron Collider (LHC) at CERN are very crucial in probing for new hypothetical particles. However, they can miss new physics effects and particles such as light and weakly coupling particles not included in the SM. This is where precision experiments are needed for complementary studies in the search for new physics.

Inspired by the discrepancies between theory and experiment for the muon anomalous magnetic moment [11] as well as between the results for the proton charge radius determined from spectroscopy of atomic hydrogen and from muonic hydrogen [12], David McKeen and Maxim Pospelov suggested to study muon physics more closely. In particular, they suggested to investigate muons interacting with thin targets in order to probe for a new light and weakly interacting particle [13]. More explicitly, they recommended an experiment where low energy negative muons are captured in a thin target with $Z \geq 30$. The muons enter directly into the atomic 2S state which preserves the longitudinal muon polarization, and they instantly undergo the $2S_{1/2} - 1S_{1/2}$ transition. During this process two photons are emitted: one when the muon enters the atom, the other one during the deexcitation. The direction in which the second photon is emitted with respect to the direction of the muon spin indicates whether or not the process is parity-violating.

So far, the direct capture of a negative muon into the 1S or 2S state has not been observed. That is why the PIENU detector was modified slightly in December 2012 and data was collected with a negative muon beam to detect the direct capture process. The procedure of this experiment, the data analysis and a comparison to the theoretical prediction are presented in the second part of this thesis.

Chapter 2

Description of the PIENU Experiment

2.1 Overview

The PIENU experiment was carried out from 2008 until 2012 in the meson hall of Canada's National Laboratory for Particle and Nuclear Physics (TRIUMF). Its cyclotron delivered a 500 MeV proton beam from which pions were produced and guided through a beamline to the PIENU detector. During an experimental run, positively charged pions entered the detector and stopped in an active target where the pion decayed to a neutrino and a positron or to a neutrino and a muon. The latter stopped within the target as well and decayed further to a positron and two neutrinos. Feynman diagrams for the decays are shown in Figure 2.1. In both cases, positrons were emitted in the final state, but their different features in time and energy were utilized to distinguish between them. Since the lifetime of a pion ($\tau_\pi = 26\,\text{ns}$) is two orders of magnitude smaller than that of a muon ($\tau_\mu = 2.2\,\mu\text{s}$), measuring the time distribution of the outgoing positrons with respect to the incoming pions indicated which type of decays occurred within the target. The left panel of Figure 2.2 shows the simulated time spectra for both decays. Furthermore, the energy spectra of the two decay modes differed substantially since one of them was a two body decay (e^+ and ν_e) at rest, whereas the other one involved three decay products (e^+, ν_e and ν_μ). The positron and neutrino from the direct pion decay

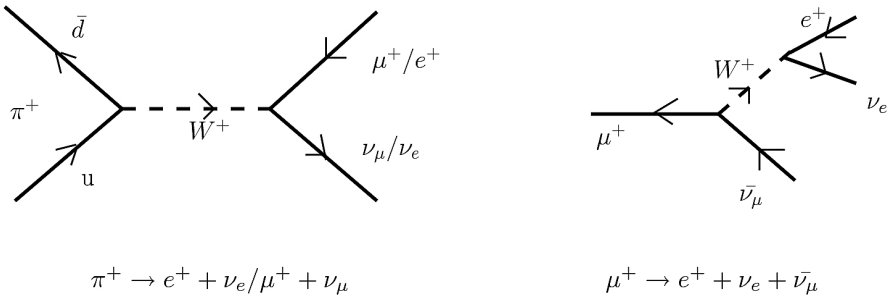

Figure 2.1: Feynman diagrams for the decay of a pion to a lepton and a neutrino (left panel) and for a muon decaying to a positron and two neutrinos (right panel).

shared the momentum of the pion's rest mass, so that in theory the positron should have had an energy of 69.8 MeV. However, because of energy deposited in the detector components, leakage out of the calorimeter, and radiative decays the energy spectrum peaked at $\sim$ 65 MeV and had a low energy tail, as shown on the right hand side of Figure 2.2. On the other hand, the energy spectrum of the positron from the muon decay, the so called Michel spectrum, had the typical broad shape of a three body decay and a sharp edge at $\sim$ 52 MeV.

In the analysis, the energy spectrum was used to divide the data sample into a low (E $<$ 50 MeV) and a high (E $>$ 50 MeV) energy part, and a simultaneous time fit was applied to these two data portions including backgrounds to determine the raw branching ratio. Corrections had to be applied to account for systematic effects such as the energy-dependent acceptance of the detector, the fact that muon decays in flight (MDIF) could reach energies above 50 MeV and were then misidentified as $\pi \rightarrow e\nu_e$ decays, and finally the leakage out of the calorimeter, the so called tail correction.

In this thesis, only the detector elements which are crucial for the study of the tail correction and for the muon capture experiment are described. For a detailed description of the theoretical background and the experimental setup of PIENU refer to Chloé Malbrunot's doctoral thesis [1].

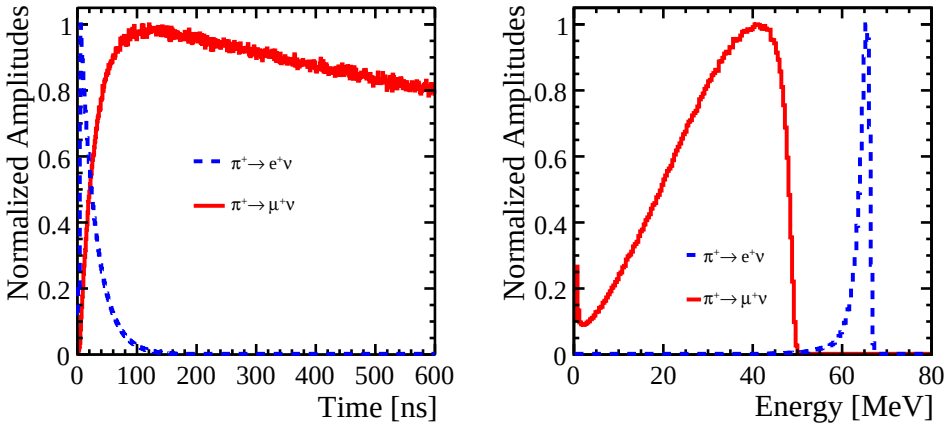

Figure 2.2: Time spectra (left panel) and energy spectra (right panel) for $\pi \rightarrow \mu \rightarrow e$ (red solid line) and $\pi \rightarrow e$ (blue dashed line) decay.

2.2 The Beamline and Detector

The cyclotron at TRIUMF produced 500 MeV protons with a Radio Frequency (RF) of $\sim$ 23.1 MHz which hit a 12 mm beryllium production target emitting various particles, among which were pions, electrons, and muons. These particles were directed towards the experimental area of PIENU through the momentum and particle selecting beamline M13 shown in Figure 2.3.

Bending magnets, quadrupoles, and a combination of slits and absorbers selected the desired momentum of 75 MeV/c. Furthermore, a degrader placed near the focus F1 caused a momentum spread between positrons, muons, and pions so that the collimator placed at focus F3 after the second bending magnet could be tuned to select pions only. Therefore, backgrounds due to positrons and muons were highly suppressed [14]. After passing through the beamline, the particles entered the PIENU detector; a diagram of its experimental set-up is shown in Figure 2.4.

The pions traversed two multi-wire proportional chambers (WC1 and WC2) for tracking purposes, then they reached a set of plastic scintillator counters; B1 and B2 were used for particle identification through energy deposit and the Time Of Flight (TOF) with respect to the cyclotron RF timing. In the active scintillator

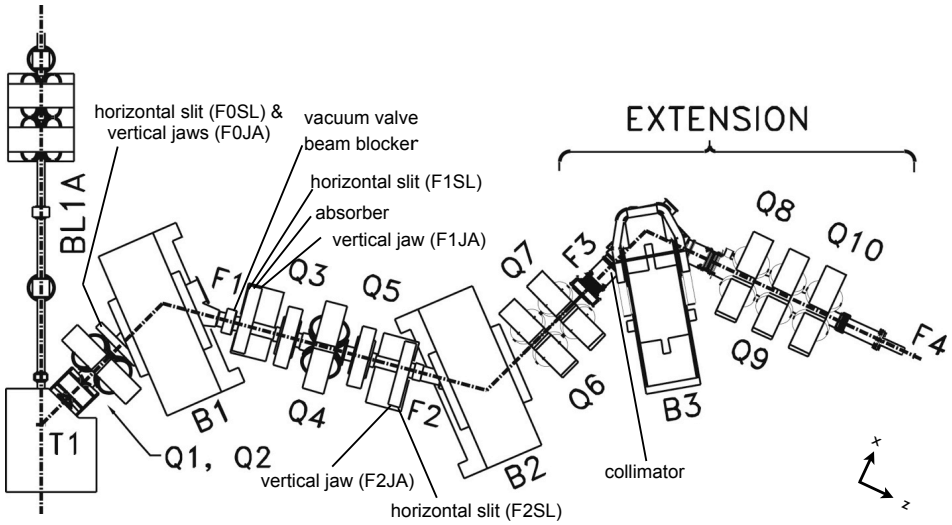

Figure 2.3: The M13 beamline at TRIUMF including the extension built in 2008. Picture taken from reference [1].

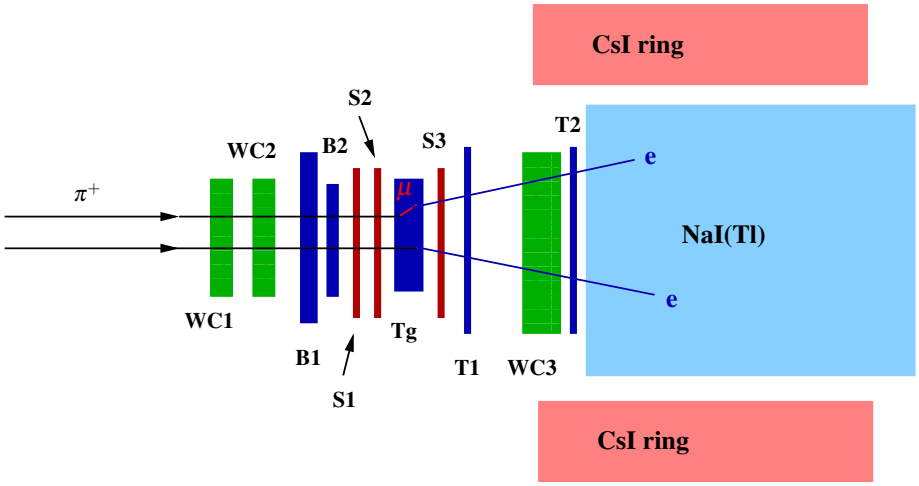

Figure 2.4: Diagram of the experimental set-up of the PIENU detector (not to scale).

target (Tg), the pions came to a stop and decayed. Two silicon strip detectors were placed before the target (S1 & S2), one behind it (S3) to reconstruct the tracks of the in- and outgoing particles. Each of these detectors consisted of two layers of strips, placed perpendicular to each other for two dimensional position information. A third wire chamber (WC3) was placed behind the target to obtain tracking in combination with S3 and to define the angular acceptance. This wire chamber was sandwiched between two more plastic scintillator counters (T1 & T2), which were used to define the trigger. After T2, the particles entered a cylindric solid (Thallium doped) Sodium Iodide (NaI(Tl)) crystal, 48 cm in diameter and 48 cm long, which served as calorimeter. Two layers of Cesium Iodide (CsI) crystals surrounded the NaI(Tl) crystal in order to reduce the amount of undetected shower leakage. Each of the plastic scintillators was read out by four Photo Multiplier Tubes (PMTs), whereas 19 PMTs were attached to the NaI(Tl) crystal for light collection and each of the 97 CsI crystals was attached to one PMT [15].

2.3 The Trigger and Data Acquisition System

An event was only recorded if an incoming pion came in coincidence with an outgoing positron. The entrance of a pion was defined by a coincidence of the beam counters B1, B2 and Tg, whereas a positron leaving the Tg in the direction of the NaI(Tl) crystal was represented by a coincidence of T1 and T2. If these two signals occurred within a time window of [-300 ns, 500 ns] the event was selected. The lower boundary of this window was chosen to characterize the background of muons present in the detector before the pion entry, and the region between 0 ns and 500 ns allowed to study the two decay modes with their different decay constants. Since the probability for $\pi \to \mu\nu_\mu$ decay is four orders of magnitude larger than that for $\pi \to e\nu_e$ decay, specialized triggers were implemented to enhance the $\pi \to e\nu_e$ decay mode. This was later taken into account when analyzing the data. Two special triggers selected $\pi \to e\nu_e$ events, the so called early and TIGC triggers. If the signal of the outgoing positron occurred between 7 ns and 40 ns the event was selected by the early trigger. In case the online sum of the energy deposited in the calorimeters was above a threshold of 46 MeV the event was recorded by the TIGC trigger. These two triggers exploited the characteristics of the positron originating

from $\pi \to e\nu_e$ decay since the pion has a short lifetime and the emitted positron left a high energy deposit in the crystals. Furthermore, the "normal" trigger defining the incoming pion and emitted positron, which recorded both $\pi \to e\nu_e$ and $\pi \to \mu \to e$ events, was prescaled by a factor of 1/16 to reduce $\pi \to \mu \to e$ events [15].

In addition to the triggers mentioned above, three more triggers were used for calibration purposes: one trigger selected cosmic-ray events for CsI calibration; a Xe lamp was flashed twice per second illuminating the CsI PMTs to monitor changes in their gains; and data collected with a beam positron trigger provided information for the calibration of the NaI(Tl) and the plastic scintillators T1 and T2 [1].

Once an event was triggered, the data was processed using a Data Acquisition System (DAQ). A 60 MHz Analog to Digital Converter (ADC) read out the signals from the CsI crystals, from each single NaI(Tl) PMT as well as from the online sum of the PMTs. Furthermore, it digitized the signals from the silicon detectors in a time window of $1\,\mu$s around the timing of the decay positron. The signals from the plastic scintillators were read out by a 500 MHz Flash Analog to Digital Converter (FADC) covering a time window of $8\,\mu$s around the pion timing. This FADC also read out the online sum of the NaI(Tl) tubes providing more samples in a longer time window than the 60 MHz ADC. The MIDAS data acquisition system [16] provided a web interface to control the data taking process. It also facilitated the monitoring process by allowing programs to check the quality of data online.

Chapter 3

Data Analysis of the PIENU Experiment

After the data collection, the stability within the recorded variables was studied for all runs and only those with smooth data taking conditions were chosen for further analysis. The procedure of extracting the branching ratio between $\pi \to e\nu_e$ and $\pi \to \mu \to e$ decays is described in this chapter.

3.1 Raw Branching Ratio and Systematic Effects

The raw signals obtained from the PMTs of each individual detector had to be calibrated in order to measure the energy deposit in MeV. The information from the cosmic ray triggered events was used to calibrate the CsI crystals by comparing the data to a detailed simulation of the system. The NaI(Tl) crystal was calibrated by using the beam positron trigger, whereas the tracking detectors' energy deposit was compared to that calculated for minimum ionizing particles and to a Monte Carlo (MC) simulation. The signal time for the beam counters B1, Target (Tg) and T1 as well as that for the NaI(Tl) crystal were either obtained from a hit-finding algorithm or from a fit of the waveform in the ADC. During the fit procedure, the waveform was compared to a template for an average PMT signal and thus the time of the maximum energy deposit was determined. In the special case of the Tg counter the fit procedure was applied for one, two, and three hits. This provided

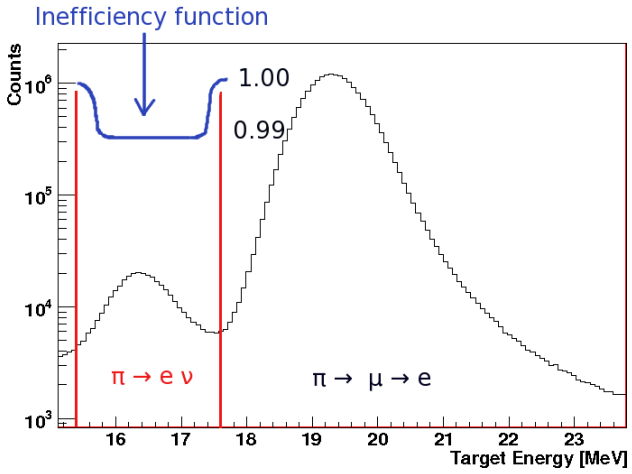

Figure 3.1: Blinding procedure: $\pi \to e\nu$ decays were selected via the energy deposit in the target by the cuts indicated by the vertical red lines, and an inefficiency function between 0.99 and 1.00 was applied to the selected events.

a handle to distinguish between the two hit $\pi \to e\nu$ and the three hit $\pi \to \mu \to e$ decays [17].

In order to minimize human bias, the data was modified to accommodate a blind analysis. As shown in figure 3.1, the $\pi \to \mu \to e$ decay deposited an extra 4 MeV of energy in the Tg compared to the $\pi \to e\nu$ decay mode due to the muon, which lost all of its energy and came to a stop within the Tg. By applying a cut on the energy deposit in the target, $\pi \to e\nu$ events were selected, and an inefficiency function between 0.99 and 1.0 was applied to this selection so that the ratio between the decay modes was altered artificially at a significant level at the precision the PIENU experiment is aiming at in the end. The value of this function was randomly chosen and is not known to the scientists involved in the analysis. Therefore, the exact result for the branching ratio cannot be compared to any known values until all of the systematic effects and backgrounds are well understood. In the end, the data is unblinded by removing the inefficiency function [18].

So as to determine the raw branching ratio, a simultaneous time fit of both the low energy region ($E_{NaI} + E_{CsI} < 50\,\text{MeV}$) and the high energy region ($E_{NaI} + E_{CsI} > 50\,\text{MeV}$) was performed, as shown in figure 3.2. The fitting functions included the exponential decays due to the lifetimes of the muon and the pion respectively, as well as a number of background shapes. These backgrounds had various origins: in the low energy region they were mainly caused by muons sitting in the detector material and decaying at a time that was not correlated to the incoming

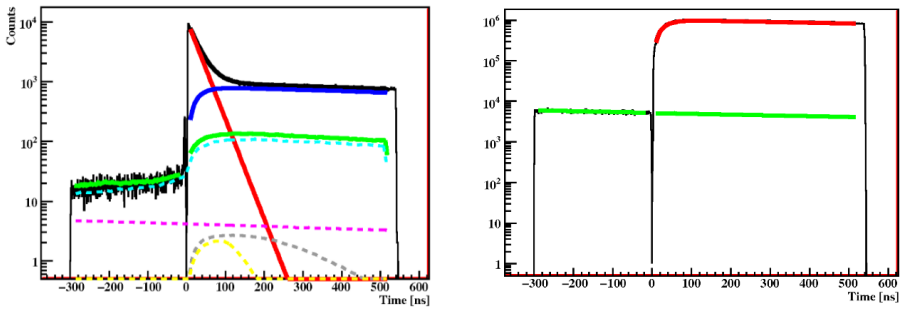

Figure 3.2: Simultaneous time fit of the high (left panel) and low (right panel) energy regions including background shapes.

pion and by pions decaying in flight prior to the arrival at the target. In the high energy region on the other hand, one of the origins was the pile up of two muon decays: one muon arriving from the beam, the other one sitting in the detector already. Other possibilities for $\pi \to \mu \to e$ decays to have an energy above 50 MeV were the simultaneous detection of the photon in a radiative muon or pion decay that increased the energy deposit in the calorimeter, and the finite energy resolution of the latter due to which some events actually located below the 50 MeV threshold were detected as higher energy events. While taking all of these backgrounds into consideration, the ratio $R = \frac{\pi \to e\nu(\gamma)}{\pi \to \mu\nu(\gamma)}$ was calculated. This was, however, the raw branching ratio that still needed to be corrected for a number of systematic effects.

One of these effects was a correction for MDIF. A positron emerging from the decay of a pion at rest and a muon in flight can have energies above 50 MeV, and its timing is shorter than the muon lifetime. Therefore, the ratio between $\pi \to e\nu_e$ and $\pi \to \mu \to e$ decays was distorted. The difference between the energy spectra for muon decays at rest (MDAR) and decays in flight is shown in figure 3.3. The correction to the branching ratio due to $\pi \to \mu \to e$ events above 50 MeV was calculated from the probability of muon decay in flight and the proportion of these events above 50 MeV, which was obtained from MC. Combining these two leads to a multiplicative correction to the branching ratio of $Corr_{MDIF} = 0.9976 \pm 0.0002$.

A second systematic effect was due to the acceptance of the detector. There

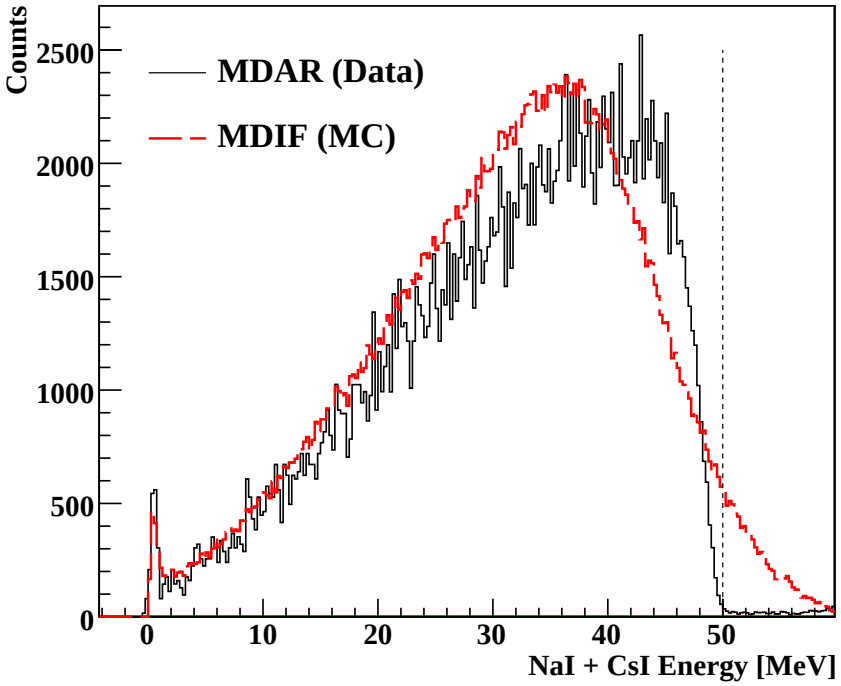

Figure 3.3: Energy deposit of the positron from muon decays at rest (solid black line) versus muon decays in flight (dashed red line). The dotted black line indicates the energy cut off at 50 MeV

were two energy dependent processes that deflected the positron after the Tg counter: Multiple scattering caused by the Coulomb force of the nucleus could deflect the path of a positron and Bhabha scattering resulted in an electron and a positron being emitted in a direction different from the one the initial positron had. In addition, annihilation in flight could occur before or in the trigger counters T1 and T2 and some low energy positrons did not reach T1 or T2. Consequently, these events did not cause a trigger. All of the processes mentioned above have energy dependent cross sections which means that the effects differ for low and high energy positrons, so a correction had to be applied to the raw branching ratio. It was calculated for an angular acceptance defined by a 60 mm radius in the third wire chamber.

Finally, a tail of $\pi \to e\nu$ events existed in the low energy part of the spectrum because of low energy photons leaking out of the calorimeters, radiative photons escaping the detector, and Bhabha scattered electrons or positrons that were not recorded in the detector system. The correction for the tail was relatively large (at the order of $\sim 2\,\%$), so it was not only determined from MC but also by data analysis. There were two approaches in estimating this correction: firstly, an estimate of the low energy tail was derived from a special measurement with 70 MeV positrons; secondly, we obtained a lower limit on the tail correction by analyzing the PIENU data set and suppressing $\pi \to \mu \to e$ decays. The procedure of estimating this lower limit is the main work for this thesis and is described in the following sections. Subsequently, the lineshape measurement and data analysis are explained and a method of combining the two is presented.

3.2 Lower Limit Determination

To estimate the fraction of $\pi \to e\nu_e$ events below 50 MeV, the so called "$\pi \to e\nu_e$ tail ", a number of suppression cuts was applied to the energy spectrum which selected mostly $\pi \to e\nu$ events and suppressed the large $\pi \to \mu \to e$ background that was present in the low energy region. What remained after these cuts was the $\pi \to e\nu$ tail buried under a background of the $\pi \to \mu \to e$ events that were not suppressed. The following sections describe the procedure of determining a lower limit on the $\pi \to e\nu$ tail as well as the corrections that had to be applied.

3.2.1 Suppressed Spectrum

The $\pi \to \mu \to e$ events in the low energy region (< 50 MeV) had to be suppressed to obtain an estimate for the tail of $\pi \to e\nu_e$ events. To do so, different observables were extracted from the data and the different properties of $\pi \to e\nu$ and $\pi \to \mu \to e$ decays were exploited to place cuts on these observables and select mostly $\pi \to e\nu$ events. To improve on the work in [1], the following cuts were studied with respect to their efficiency (ratio of high energy events before and after the cut) and the low energy fraction (number of low energy events divided by all events). During the optimization process, the efficiency for each cut was maximized while minimizing the low energy fraction and keeping enough events to have sufficient statistics.

As mentioned in section 2.1, the time spectra of $\pi \to e\nu$ and $\pi \to \mu \to e$ decays differ substantially. This fact was used to set a cut on the decay time between the incoming pion and the outgoing positron from the Tg scintillator. The requirement of a short decay time of the pion mostly selected $\pi \to e\nu$ events, so the first requirement for the suppressed spectrum was: $4\,\text{ns} < t < 35\,\text{ns}$, this selection resulted in a decrease in the low energy fraction to 98.83 %, which is 0.2 % lower than in reference [1], while remaining at the same efficiency.

The second major difference between the two decay modes was their energy deposit in the upstream detectors B1, B2 and Tg. We call the cumulative energy deposit in these three detectors the "total beam energy". As shown in figure 3.4, the extra 4 MeV energy deposit from the muon clearly separated the two decays. So a cut on the total energy between 15.9 MeV and 16.8 MeV suppressed more $\pi \to \mu \to e$ decays. These boundaries ensured a more symmetric cut on the total energy than in reference [1] and the low energy fraction was decreased by 4 % to 26.55 %.

The difference in the total energy spectrum was also exploited in a different way: As mentioned in section 3.1, a fit to the waveform in the target was performed to check for a two hit (pion and positron) or three hit (pion, muon, and positron) event [1]. The χ^2 for each case provided information on the goodness of the fit and served as a handle to determine which decay occurred. The difference between the values of χ^2 for the two and three hit fits is shown in figure 3.5 versus the total energy. There is a clear separation between $\pi \to e\nu$ and $\pi \to \mu \to e$ events depending on the sign of the difference, defined as $\Delta\chi^2 = \chi^2_{2hits} - \chi^2_{3hits}$. A cut on this variable at $\Delta\chi^2 < 0$ extracted $\pi \to e\nu$ events, this selection differs slightly from the one in [1].

The cuts mentioned above removed most of the background due to decays at rest. However, some $\pi \to \mu \to e$ events involved pion decays in flight (PDIF) before the target and had a similar energy deposit in the target as a $\pi \to e\nu$ event, but a different signature in the upstream tracking detectors. As shown in figure 3.6, events in flight entered the target at an angle. This angle was calculated from the coordinates in the tracking detectors and is shown in figure 3.7 for PDIF and pion decays at rest (PDAR). Placing a cut for $\theta < 12^\circ$ suppressed the decays-in-flight of $\pi \to \mu \to e$ events.

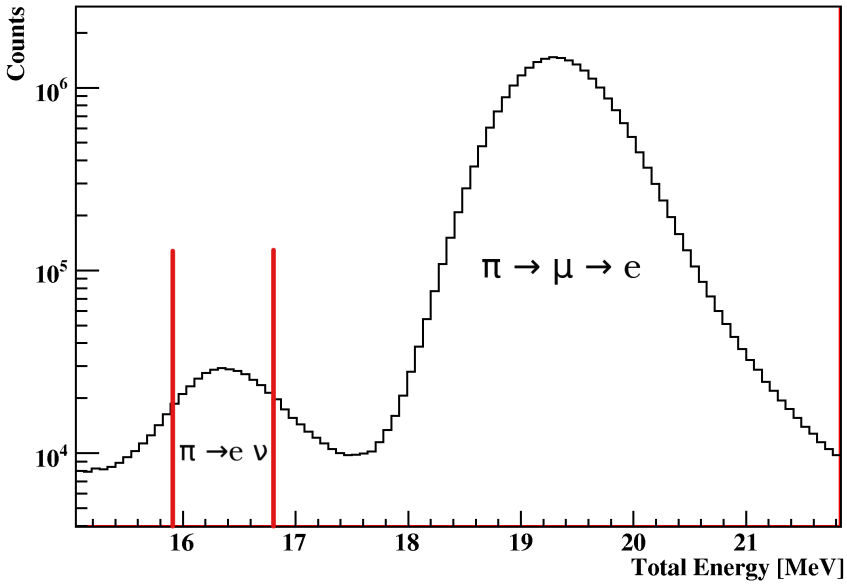

Figure 3.4: Energy deposit in the upstream tracking detectors ("total energy", solid black line) and suppression cut selecting $\pi \to e\nu$ events (bold red lines).

However, the angle cut did not suppress the decays in flight occurring after the upstream tracking detectors. Since muons originating from a pion decay in flight had a higher energy than those from decays at rest, some of them leaked out of the target and reached the silicon detector S3. They had a greater energy deposit in the silicon than a positron from a pion or muon decaying in the target. Therefore, requiring a low energy deposit in the x- and y-planes of S3 according to $E_X^2 + E_Y^2 < (1.2\,\mathrm{MeV})^2$ suppressed the decays in flight taking place after the upstream tracking detectors.

Table 3.1 summarizes the cuts described above, which produced the suppressed spectrum shown in figure 3.8. For each cut, the fraction of low energy events (LE fraction) is included, defined as the number of events below 50 MeV divided by all events.

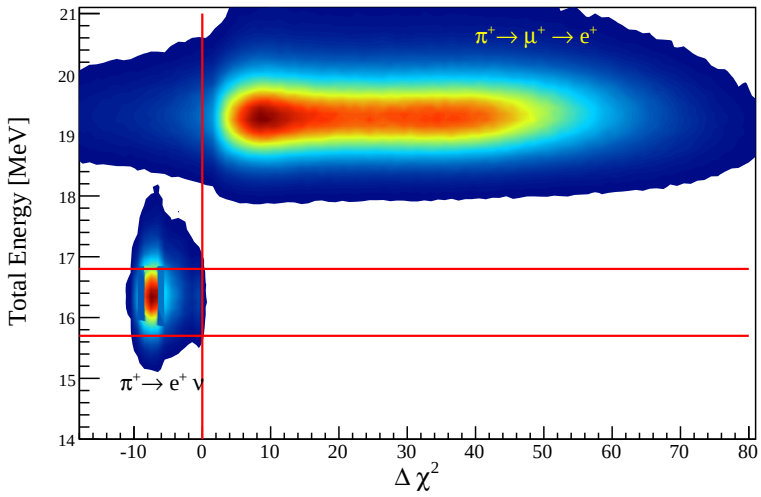

Figure 3.5: Energy deposit in the upstream counters (B1, B2, Tg) versus $\Delta\chi^2 = \chi^2_{2hits} - \chi^2_{3hits}$. The red lines indicate the cut on $\Delta\chi^2$ and the energy deposit. (Figure taken from ref. [1].)

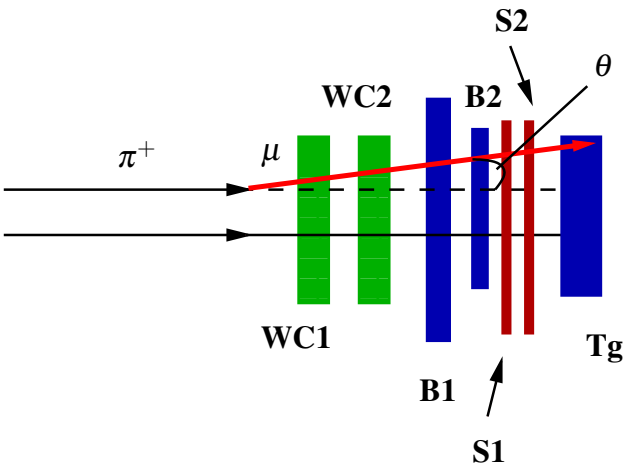

Figure 3.6: Schematic drawing of a PDIF in front of the target with its decay angle compared to the straight track of a pion stopping in the target.

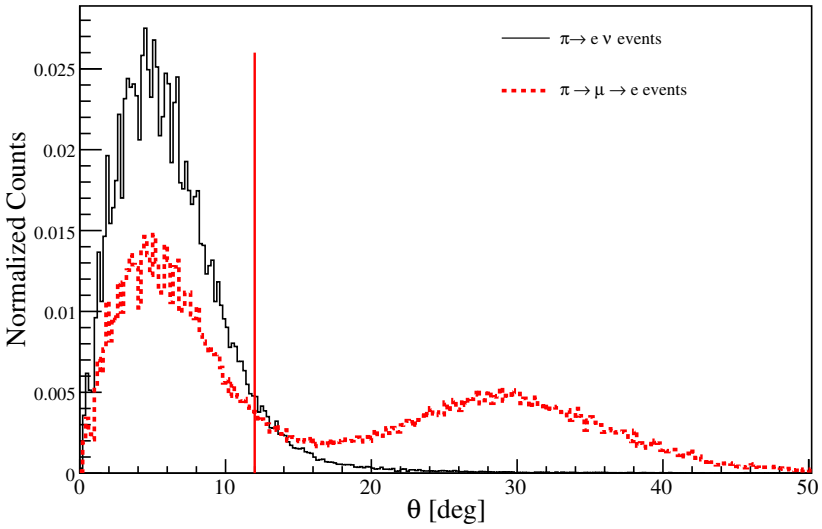

Figure 3.7: Angle between the particle track and the beam direction in solid black for $\pi \to e\nu$ ($E_{NaI} > 55\,\mathrm{MeV}$) events, in dashed red for $\pi \to \mu \to e$ ($E_{NaI} < 30\,\mathrm{MeV}$) events. The vertical red line indicates the cut placed at $\theta = 12°$. Figure taken from ref. [1]

Variable	Cut	LE fraction [%]
Time	$4\,\mathrm{ns} < t < 35\,\mathrm{ns}$	98.83
Tg Energy	$15.9\,\mathrm{MeV} < E < 16.8\,\mathrm{MeV}$	26.55
Angle θ	$\theta < 12°$	14.06
Energy in x- and y-plane of Si3	$E_X^2 + E_Y^2 < (1.2\,\mathrm{MeV})^2$	12.91
Pulse Shape in Tg	$\Delta\chi^2 < 0$	12.87

Table 3.1: Summary of the cuts used to produce the suppressed spectrum. The low energy fraction (LE fraction) is defined as the number of low energy events divided by the total number of events after each cut.

3.2.2 Determining the Lower Limit

The cuts described above suppressed most of the $\pi \to \mu \to e$ events in the low energy region. However, a fraction of them still remained. Therefore, the tail of $\pi \to e\nu_e$ events in this energy region had to be extracted. To calculate this tail, we first estimated the amount of $\pi \to \mu \to e$ events within the suppressed spectrum

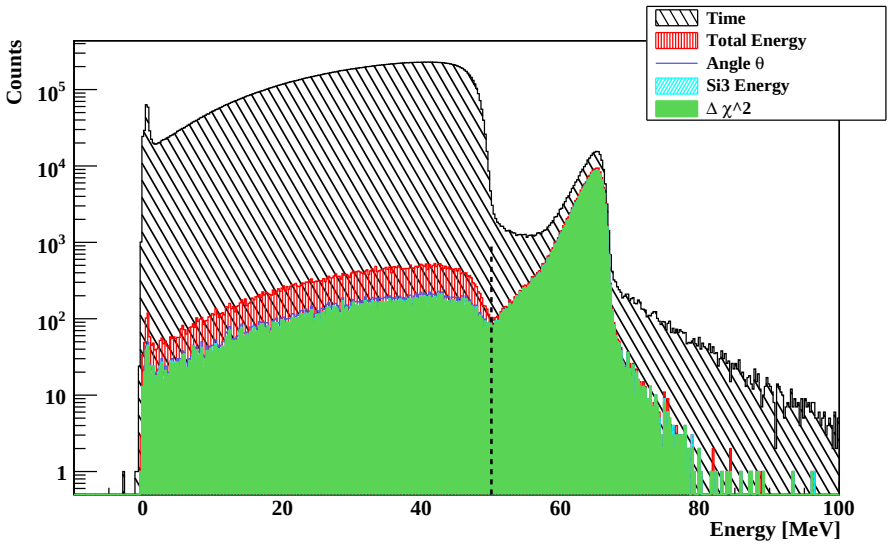

Figure 3.8: Effect of the different suppression cuts on the energy spectrum.

by assuming that there was no tail present below an energy i which was lower than the Michel edge ($i < 50\,\text{MeV}$), and by comparing its shape to the Michel spectrum below this energy i. Subsequently, we subtracted this amount from the total number of events in the suppressed spectrum. Due to the assumption of no tail below the energy i, we obtained a lower limit on the amount of $\pi \to e\nu_e$ events below 50 MeV; the integral up to i was called a[i]. The total number of $\pi \to \mu \to e$ events in the low energy region was evaluated from the region below i by integrating the Michel spectrum up to the same energy i, this integral was called b[i]. b[i] divided by the total number of events present in the Michel spectrum below 50 MeV, called B, is equal to the fraction of the total number of events that a[i] should represent. a[i] divided by this ratio provided us with the total number of events below 50 MeV in the suppressed spectrum originating from $\pi \to \mu \to e$ background. By subtracting this number from the number of events in the low energy part of the suppressed spectrum (A), we obtained a lower limit on the tail fraction, called Ll[i] [1]:

$$\text{Ll[i]} = \text{A - a[i]}\frac{\text{B}}{\text{b[i]}} \tag{3.1}$$

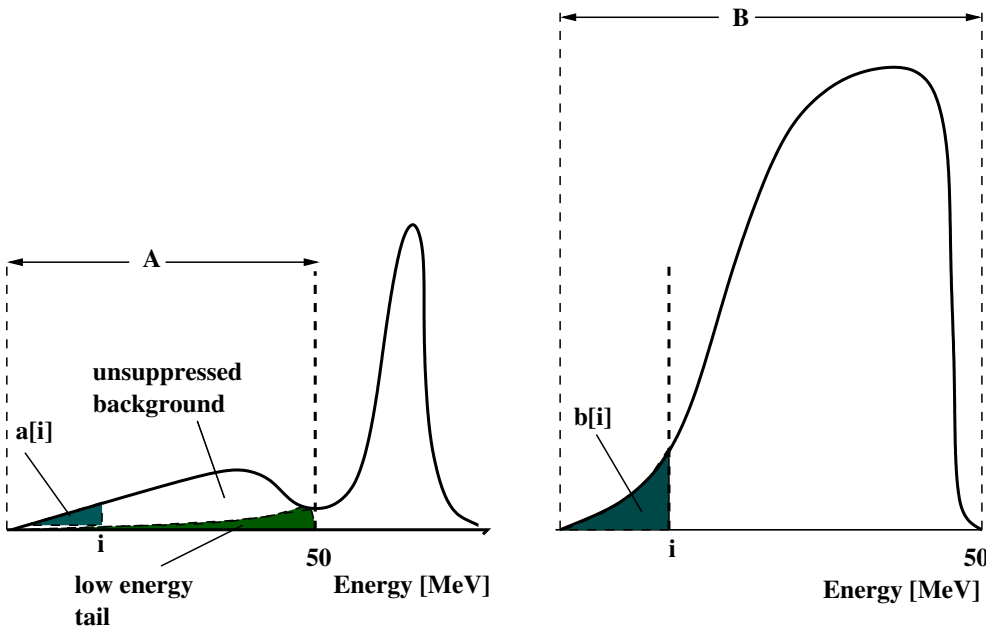

Figure 3.9: Evaluation procedure for the lower limit. Left: suppressed spectrum with the low energy tail in green and the integration region a[i] in blue. Right: Michel spectrum with the integration region b[i] in blue. Dashed lines indicate integration limits. A and B are the integrals up to 50 MeV of the suppressed spectrum and the Michel spectrum respectively.

Figure 3.9 illustrates the different integrals and the evaluation procedure. The Michel spectrum was obtained from the data by applying the same suppression cuts as for the suppressed spectrum, the only differences were the timing cut and the pulse shape cut as the latter would introduce time distortions. For a sample of $\pi \to \mu \to e$ decays, $t > 100\,\text{ns}$ was required instead of the early cut for $\pi \to e\nu$ events.

After calculating the lower limit for the upper integration limit i varying between 1 MeV and 50 MeV, we chose the highest of these values to avoid an underestimation. Figure 3.10 shows the dependence of the lower limit on the upper integration limit i. The assumption of zero tail is a good approximation at low energies, although the statistics in this region are poor. At higher energies, the actual tail is non-zero but there are more events in the spectra. By construction, the lower

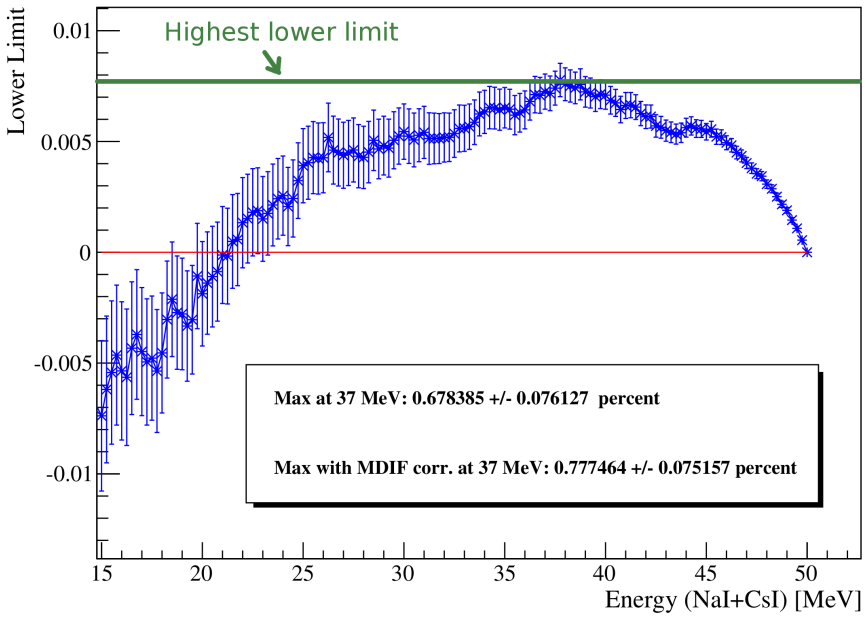

Figure 3.10: Lower Limit versus upper integration limit i. At 50 MeV the lower limit is zero, as indicated by the red line. The MDIF correction has been applied for this figure.

limit is zero at 50 MeV since a[i] = A and b[i] = B; the red line in figure 3.10 indicates this. Therefore, a value at an intermediate energy is the best approximation for the lower limit. The MDIF correction described in the next section has been applied to the lower limit in figure 3.10.

As shown in figure 3.10 the lower limit takes negative values below an upper integration limit of ~ 20 MeV. This occurs because of an oversubtraction in the lower limit formula 3.1 when the $\pi \to \mu \to e$ background estimate is too large. However, the effect can be explained by statistical fluctuations as outlined in section 3.2.8.

The tail fraction was calculated by dividing the lower limit Ll[i] by the total number of events in the suppressed spectrum and was used as a multiplicative correction to the raw branching ratio.

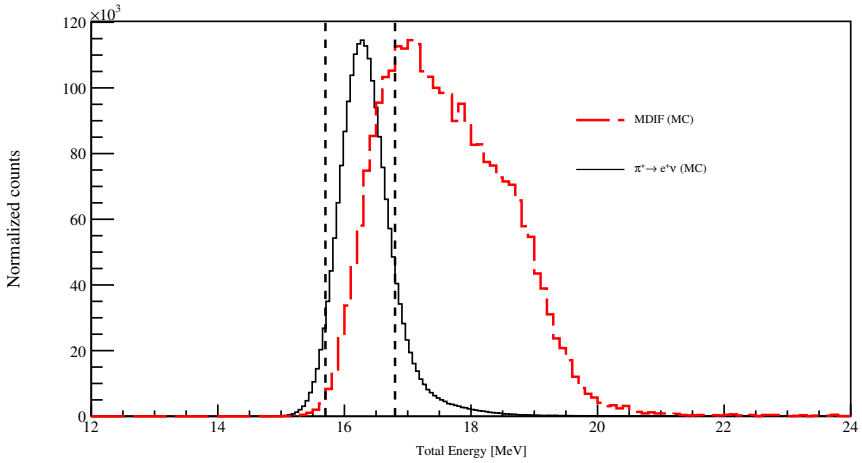

Figure 3.11: Energy deposit in the detectors upstream of the target for $\pi \to e\nu$ decays in solid black and for MDIF events in dashed red. The dashed vertical lines indicate the cut on the energy deposit. Figure taken from ref. [1]

3.2.3 Muon Decay in Flight Correction to the Lower Limit

As described in the previous section, we used a selection of late events to obtain the background shape of $\pi \to \mu \to e$ decays. However, this left out the MDIF which could not be selected separately within the data but were present in the suppressed spectrum. Figure 3.11 shows the energy deposit of MDIF compared to that of $\pi \to e\nu_e$ events and the effect of the total energy cut.

We included those events in the background estimation by applying a correction to the background Michel spectrum based on an energy spectrum for MDIF obtained from MC. [1] In order to add the two spectra with the correct proportions, we calculated the fraction of MDIF events compared to PDIF. A fit to the energy and time distributions of the suppressed spectrum provided information on the composition of the suppressed spectrum in terms of MDIF, PDIF and the $\pi \to e\nu$ tail. By

[1] Note that there are two different corrections for MDIF: The one mentioned in section 3.1 is applied to the branching ratio to account for the fact that some MDIF events have energies above 50 MeV and are therefore contributing to the "wrong" part of the ratio. The correction described in this section corrects the lower limit for the fact that MDIF events are not included in the selection of late events for the background spectrum, even though they are present in the suppressed spectrum.

minimizing the χ^2 for both the energy and the time distribution simultaneously, the fitting procedure determined the most likely composition of the suppressed spectrum. The shapes used in the fit were the MDIF distribution obtained from MC, the $\pi \to e\nu$ tail above 50 MeV from MC and the PDIF spectrum originating from the late muon selection in the data used as background spectrum in the lower limit method.

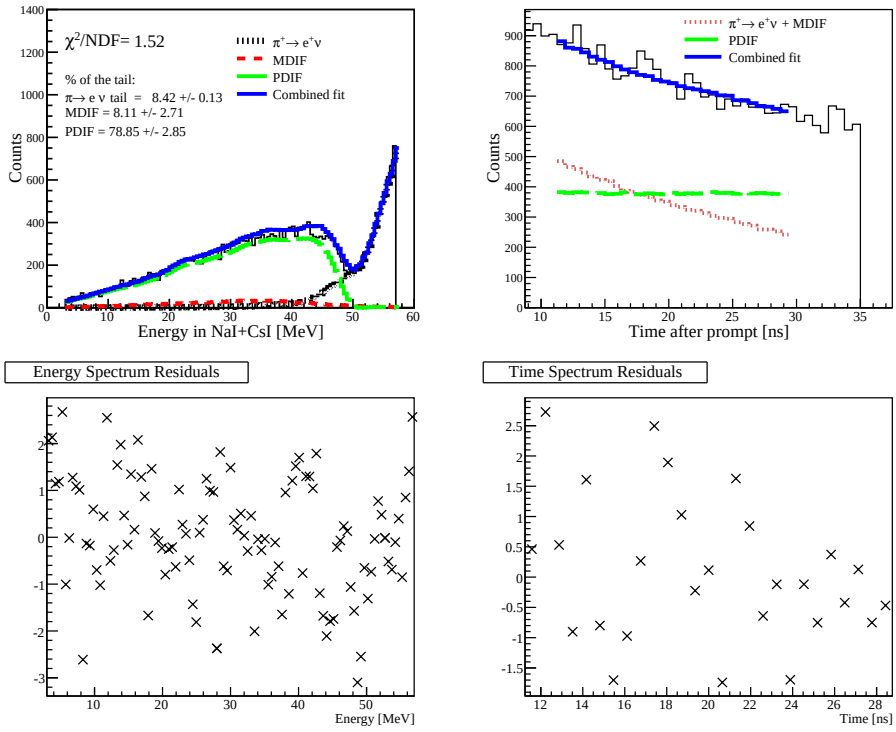

Figure 3.12: Upper panel: Simultaneous fit to the energy (left) and time (right) distributions of the suppressed spectrum. The different contributions of PDIF (green), MDIF (red) and $\pi \to e\nu$ tail (black) as well as the combined fit (blue) are shown. The percentages indicate the amount of each process within the suppressed spectrum. Lower panel: Residuals from the energy (left) and time (right) spectra.

Figure 3.12 shows the result of the fit with the contributions of the different processes to the suppressed spectrum. The value of the combined χ^2 divided by

the Number of Degrees of Freedom (NDF) $\chi^2/NDF = 1.52$ indicates that there is still room for optimization within this fitting procedure. Studies have shown that the result of the fit depends largely on the fitting range as well as the $\pi \to e\nu$ tail spectrum. The upper limit of the energy range used for the fit shown in figure 3.12 is 57 MeV, when decreasing the upper limit to 55 MeV, the MDIF fraction takes a value of 7.8 %, and for an upper limit of 60 MeV the fraction is 5.0 %. This indicates that the fit is not stable with respect to the energy range used for fitting. Additionally, the MC simulation does not reproduce the photonuclear interactions correctly at present time. These two issues, as well as the fact that the PDIF spectrum has low statistics since it is obtained from the data, can cause the value of χ^2/NDF to be larger than one.

From this fit, we extracted the ratio of MDIF to PDIF $\alpha = 0.10 \pm 0.03$. The uncertainty was calculated from the errors determined within the fitting procedure. Subsequently, the MDIF spectrum was added to the background spectrum with this proportion and the resulting spectrum was used to determine the integrals B and b[i] in the lower limit formula 3.1.

We checked the amount of MDIF predicted by the fit by calculating the fraction of MDIF to $\pi \to e\nu$ events. According to the MC simulation, 15.4 % of MDIF survived the Tg energy cut. The probability for MDIF is $8 \cdot 10^{-6}$, as calculated in [1]. Assuming the theoretical branching ratio between $\pi \to e\nu$ and $\pi \to \mu \to e$ events of $1.24 \cdot 10^{-4}$, we estimated the amount of MDIF versus $\pi \to e\nu$ events, called Q, knowing that the Tg cut had an efficiency of 89.25 % as follows:

$$Q = \frac{8 \cdot 10^{-6} \times 0.154}{0.8925 \times 1.24 \cdot 10^{-4}} = 1.11 \times 10^{-2}. \tag{3.2}$$

Since the fraction of low energy events compared to the total number of events in the suppressed spectrum is 12.87 %, $1.11/12.87 = 8.65$ % of these events are due to MDIF. This agrees well with the fraction determined from the fitting procedure.

3.2.4 Radiative Decay Correction

The lower limit method is based on the assumption that there is no tail at low energies and that it emerges at intermediate energies. As described above, the

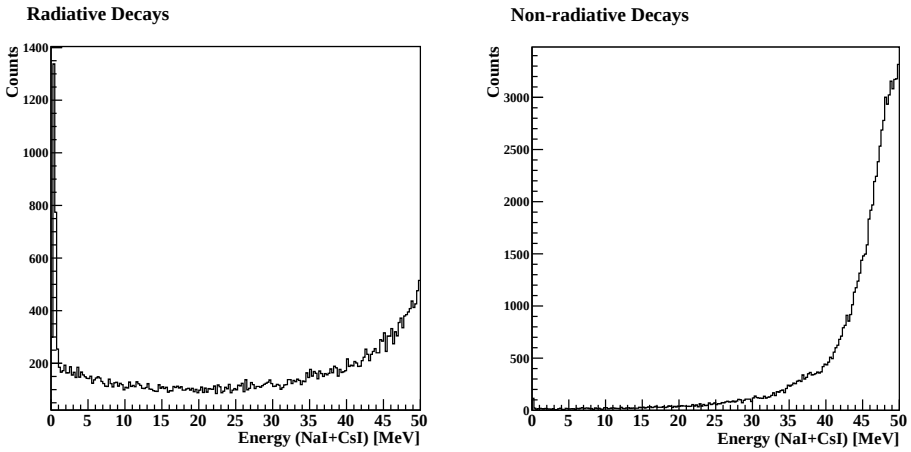

Figure 3.13: Low energy part of the Monte Carlo $\pi \to e\nu$ spectrum. Left panel: Radiative decays only. Right panel: Non-radiative decays only.

highest value for the lower limit is chosen, which is 37 MeV. Consequently no tail is expected below this energy. However, MC studies showed that the spectrum of $\pi \to e\nu\gamma$ decays (so called radiative decays) differs from that of $\pi \to e\nu$ decays. In the radiative case there is an excess of events around 1 MeV and a constant tail exists below 40 MeV due to events where the photon was missed in the NaI(Tl); this tail is shown in figure 3.13. On the other hand, the tail consisting of non-radiative decays only, shown in the right panel, becomes negligible at very low energies. To account for this difference, an additional term was introduced to the lower limit formula (see equation 3.1), which corrected for the radiative decays. This correction was not applied in reference [1]. The non-zero component at low energies was described by a correction to the lower limit formula by adding a term r[i]:

.

$$\text{Ll[i]} = \text{A - (a[i]-r[i])}\frac{\text{B}}{\text{b[i]}}, \tag{3.3}$$

where r[i] is the amount of the radiative decay spectrum integrated up to the energy i. The shape of radiative decays from MC was used to determine the integral r[i];

the spectrum was scaled to the $\pi \to e\nu$ peak of the suppressed spectrum. The scaling factor was then multiplied by 6.2 % since this is the fraction of radiative decays compared to the total of $\pi \to e\nu$ events [2].

The additional term accounted for the fact that the portion of radiative decays below 37 MeV would otherwise be counted as background resulting in an underestimation of the lower limit. After applying this correction, the shape of the tail fraction depending on the integration energy i did not approach zero at 50 MeV any more. In the limit of $i = 50\,\text{MeV}$, $a[i] = A$, $b[i] = B$, and $r[i] = R$, therefore the value of the tail fraction at 50 MeV was equal to the amount of radiative decays below 50 MeV. This is indicated by the red line in figure 3.14, which implies that there is a contribution of 0.32 % radiative decays below 50 MeV.

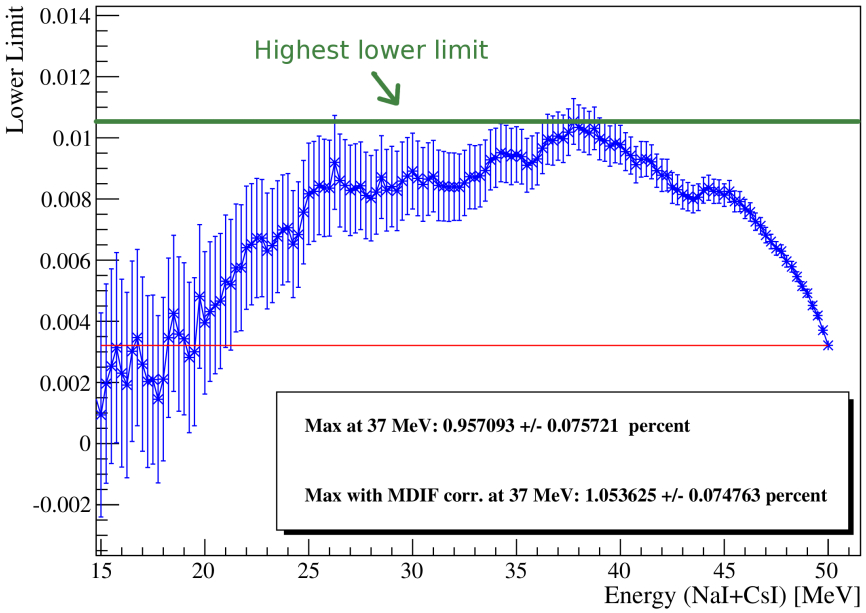

Figure 3.14: Lower limit shape with radiative decay correction (blue graph). Red Line: Value of tail fraction at 50 MeV.

3.2.5 Bhabha Correction

The cut applied on the total energy deposit of the upstream detectors removed events with an energy deposit below 15.9 MeV and above 16.8 MeV, therefore selecting most of the $\pi \to e\nu$ events. However, a portion of the $\pi \to e\nu$ events underwent Bhabha scattering in the target. This caused additional energy to be deposited in the detectors by the scattered electron which is why the energy deposit of Bhabha events was greater than that of non-scattered events. These Bhabha events were cut out by the selection cut despite the fact that they contributed to the low energy tail. Consequently, a correction was applied to the lower limit, which added back the portion of Bhabha events that were removed by the total energy cut.

According to an MC simulation, the correction amounts to $(1.186 \pm 0.013(\text{stat}) \pm 0.119(\text{sys}))\,\%$. Conservatively, the systematic uncertainty was estimated to be 10 % of the correction itself. For details on the Bhabha correction and its corresponding error as well as a comparison with Bhabha events selected within the data, refer to the PIENU technical report [19].

3.2.6 Error Estimation for the Lower Limit

For an estimate of the uncertainty of the lower limit, both the statistical and the systematic error were calculated. This procedure differs from reference [1].

Statistical Error

We estimated the statistical error on the tail fraction by assuming that the number of high energy events (HE) is Poisson-distributed, whereas the ratios of a[i] and A, b[i] and B, and r[i] and A follow a Binomial distribution since a[i], b[i] and r[i] are small samples of A and B. The expression of the lower limit in equation 3.3 can be rewritten in terms of efficiencies in the following way:

$$Ll[i] = A - (a[i] - r[i])\frac{B}{b[i]} = A\left(1 - \frac{\varepsilon_a}{\varepsilon_b} + \frac{\varepsilon_r}{\varepsilon_b}\right) \tag{3.4}$$

$$\varepsilon_a = \frac{a[i]}{A},\ \varepsilon_b = \frac{b[i]}{B},\ \varepsilon_r = \frac{r[i]}{A} \tag{3.5}$$

Assuming a Binomial distribution for all of the efficiencies, we obtained the following uncertainty on the tail fraction TF:

$$\delta TF = \sqrt{\left(\frac{HE}{(Ll[i]+HE)^2}\cdot\delta Ll[i]\right)^2 + \left(\frac{Ll[i]}{(Ll[i]+HE)^2}\cdot\delta HE\right)^2} \tag{3.6}$$

Systematic Error

The uncertainties of the MDIF and radiative decay corrections as well as the (in)stability of the tail fraction with respect to rebinning introduced systematic uncertainties. Those were determined by calculating the TF for the different scenarios and taking the largest difference within the tail fraction δTF which was assumed to be the systematic error.

- vary MDIF coefficient $\alpha = (0.10 \pm 0.03)$ within errors: $\delta TF = 0.07\,\%$
- vary radiative decay contribution of $(6.2 \pm 0.2)\%$ within errors: $\delta TF = 0.02\,\%$
- rebin all histograms by factors of 2,4,6: $\delta TF = 0.01\,\%$

When summed up in quadrature, those effects resulted in a systematic error of 0.07 % (absolute error on the tail fraction). This provided us with a lower limit on the tail fraction with statistical and systematic uncertainty:

$$TF < (1.05 \pm 0.07(stat) \pm 0.07(sys))\,\%$$

Adding the Bhabha correction mentioned in section 3.2.5, resulted in:

$$\boxed{TF < (2.24 \pm 0.07(stat) \pm 0.14(sys))\,\%}$$

3.2.7 Consistency Checks

The branching ratio, including all its corrections, is being studied with respect to systematic effects before unblinding the data set. These systematic effects include the energy cut off between the low and high energy region and the definition of acceptance. Therefore, these studies were also performed on the lower limit on the tail fraction itself in order to apply the varied correction to the branching ratio. The results for the systematics checks as well as a more detailed description of studies on the lower limit are contained in a PIENU technical report [20].

3.2.8 Statistical Effects

In order to understand the impact of statistical fluctuations on the shape of the lower limit curve, MC simulated spectra were used to calculate the lower limit multiple times and to compare the behaviour of the curves. The suppressed spectrum was constructed by adding 87 % of the $\pi \to e\nu$ tail to 13 % of the Michel spectrum as background. These numbers correspond to the percentages in the suppressed spectrum obtained from data (compare to table 3.1). In order to introduce statistical fluctuations, a histogram was filled randomly using the MC spectrum as a probability density function. The number of entries in the data spectrum determined the number of times the filling procedure was repeated. This ensured approximately the same level of statistical fluctuation in the simulated spectrum as in the data spectrum. This procedure was repeated 1000 times, calculating the lower limit every time, producing a distribution of lower limit values. Figure 3.15 shows the lower limit curve for four statistically independent samples, each of which shows a different behaviour at low energies. This indicates that the decrease of the lower limit shape from data towards low energies can be explained by statistical fluctuations.

3.3 Lineshape Measurement

Complimentary to the estimation of the $\pi \to e\nu$ tail via the lower limit method, Tristan Sullivan determined an estimate of the tail using results from a special measurement from September 2011 [2]. With a 70 MeV/c positron beam, the crystal response function was measured by directing the particles at the NaI(Tl) at various

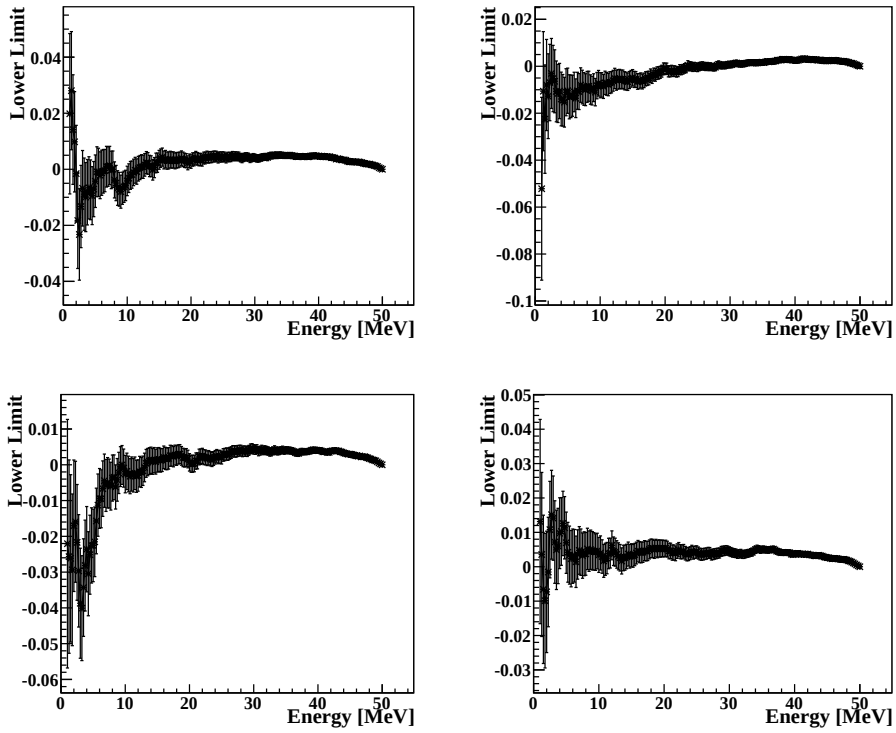

Figure 3.15: Lower limit shape for four statistically independent samples produced from MC.

angles. Only the three wire chambers and the counter T2 were used to characterize the beam in order to reduce any scattering effects. This special setup imitated the positrons emitted from the target at different angles and was therefore suitable to estimate the low energy tail of $\pi \to e\nu$ decays. Figure 3.16 shows the measured energy spectrum at 0° with selection cuts applied to choose positrons only.

The bumps on the left side of the positron beam peak at 68 MeV are due to photonuclear interactions in the NaI that resulted in one, two, or three neutrons escaping the crystal and carrying away ~ 9 MeV each [21]. Because of these interactions, the energy deposit of some positrons with an energy above 50 MeV was measured to be lower since the energy deposit detected by the calorimeter was missing the energy of the escaped neutrons. It was therefore important to take this

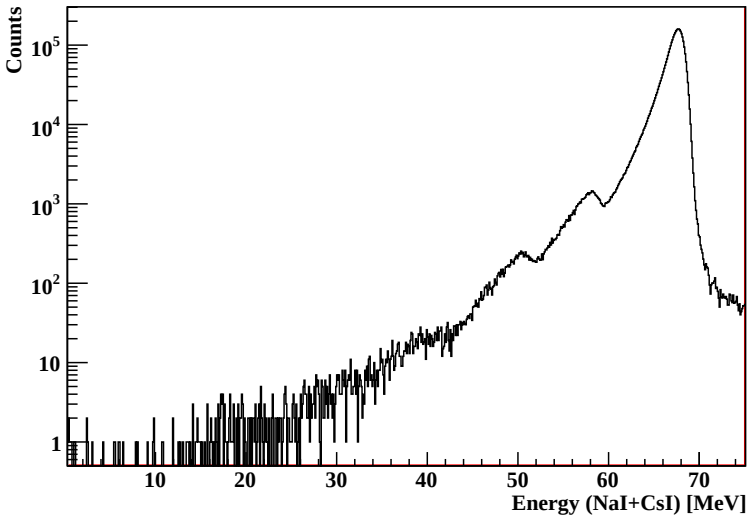

Figure 3.16: Energy spectrum of a 70 MeV positron beam aimed at the center of the NaI(Tl) crystal at 0°. Cuts are applied to select positrons only. The "bumps" originate from one, two, and three neutrons escaping the crystal after photonuclear interactions.

effect into account when estimating the low energy tail. Some differences between the actual PIENU experiment and the special run had to be considered when calculating the tail fraction: since some of the detectors were removed for the lineshape measurement, less material was present in the path of the beam, resulting in less degradation in energy and less scattering effects. Also, the positron beam did not imitate the decay positrons exactly as differences arose from spatial and momentum divergence in the beamline as well as imprecision in the setup and uncertainty in the information from the detectors that were used for the lineshape analysis. Only a simulation could overcome these differences. However, the escaping neutrons, which were first observed in the PIENU experiment, were not sufficiently well reproduced by the GEANT4 simulation used for this study. Therefore, the simulation was corrected for the photonuclear interactions by studying the difference between a simulation of the lineshape measurement and the lineshape.

Comparing the lineshape spectrum at 0° (figure 3.16) to the spectrum at 48°

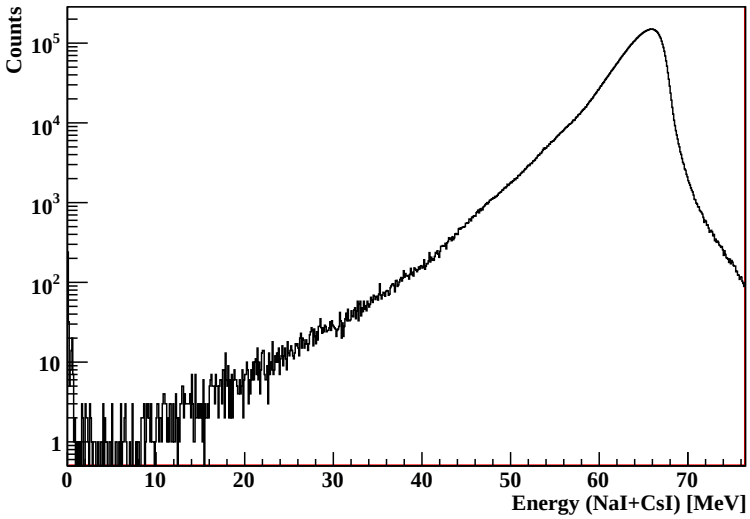

Figure 3.17: Energy spectrum of a 70 MeV positron beam aimed at the center of the NaI(Tl) crystal at 48 °.

(figure 3.17) illustrates the difference in tail fraction for different incident angles. Consequently, the fraction was determined as a function of angle, which is shown in figure 3.18 for the case when only considering the energy deposit in the NaI(Tl) and when including the CsI energy as well. In the latter case, a considerable amount of leakage out of the NaI(Tl) at higher angles is detected by the CsI. The weighted average of the NaI(Tl) plus CsI tail fraction within the acceptance region was used as correction to the simulation.

This correction also accounted for the crystal resolution of the NaI(Tl) detector as measured in the lineshape setup. The simulation provided us with a tail fraction of 1.93 % consisting of leakage out of the crystal, Bhabha events and radiative decays. The difference in tail fractions between the lineshape data and the lineshape simulation produced a correction of + 0.32 %, resulting in a tail fraction of [2]

$$TF = (2.25 \pm 0.06)\,\%.$$

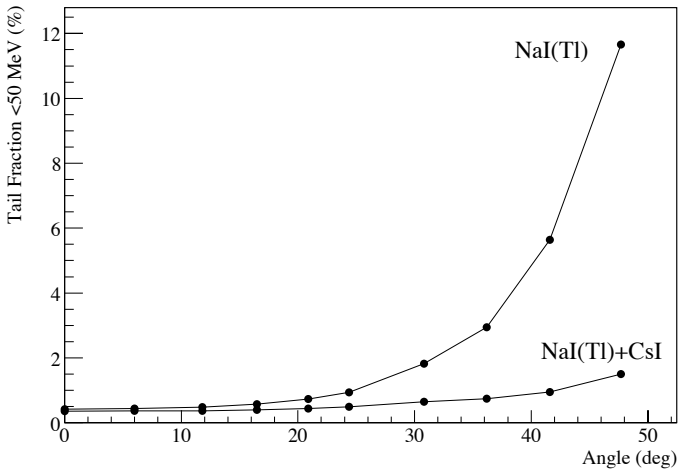

Figure 3.18: Lineshape tail fraction estimate as a function of angle for the energy deposit in the NaI(Tl) only, and for the combination of NaI(Tl) and CsI.

Taking into account the scattering in the beamline and momentum dispersion, this estimate could be considered as an "upper limit" of the tail fraction. However, a simulation of the M13 beamline using the program g4beamline was used to study the scattering effects. Before entering the PIENU detector the fraction of positrons below 52 MeV was found to be 0.03 % for a radial cut of 22 mm, which is the same as the selection cut used when analyzing the lineshape data [22]. Since this value is smaller than the uncertainty on the tail fraction estimated from the lineshape measurement, the scattering effects in the beamline are considered negligible. However, this should still be confirmed by analysis of special runs that were taken to characterize the beamline effects.

3.4 Combination of Lineshape Measurement and Lower Limit

The lineshape measurement and the lower limit were combined into one estimate of the low energy tail fraction. Taking into account their respective probability functions, we obtained a combined estimate for the probability function of the tail

fraction [23]. In the previous chapters we calculated the values of the tail fraction and the lower limit (TF and LL) with their corresponding uncertainties:

$$TF = (2.25 \pm 0.06)\,\% \tag{3.7}$$

$$LL = (2.24 \pm 0.07(stat) \pm 0.14(sys))\,\% = (2.24 \pm 0.14)\,\% \tag{3.8}$$

We assumed that the estimated uncertainties for both values are distributed according to a Gaussian function. Consequently, the value and its uncertainty correspond to the mean $\bar{x}$ and the variance σ of a Gaussian distribution:

$$f(x) = e^{-\frac{1}{2}\left(\frac{x-\bar{x}}{\sigma}\right)^2} \tag{3.9}$$

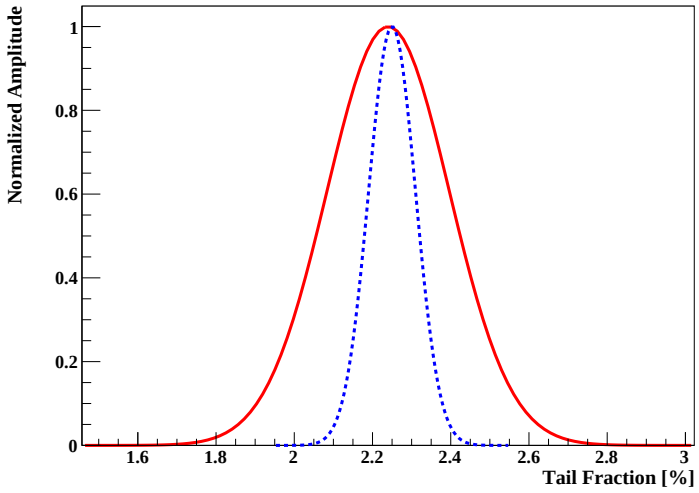

Figure 3.19: Probability distributions of the tail fraction estimate from the lineshape measurement (dotted blue line) and the lower limit (solid red line) assuming they have a Gaussian shape.

The distributions for both measured limits are shown in figure 3.19. The probability of the true value to be x corresponds to $f(x) \cdot x$. The physical meaning of

the lower limit is that the tail fraction should take a value higher than the lower limit itself. Since the probability for the true value to take the value x accumulates from all of the lower values, the integral up to x corresponds to the acceptance at that point. Therefore, we calculated the probability region for the lower limit via the error function

$$f(x) = erf(x) = \frac{2}{\sqrt{\pi}} \int_0^x d^{-t^2} dt. \tag{3.10}$$

Substituting $\sqrt{2}t = \frac{x-\bar{x}}{\sigma}$, this corresponds to the integral of the Gaussian distribution, up to a normalization constant. The allowed regions for the lineshape estimate and the lower limit are shown in figure 3.20 in blue and red respectively.

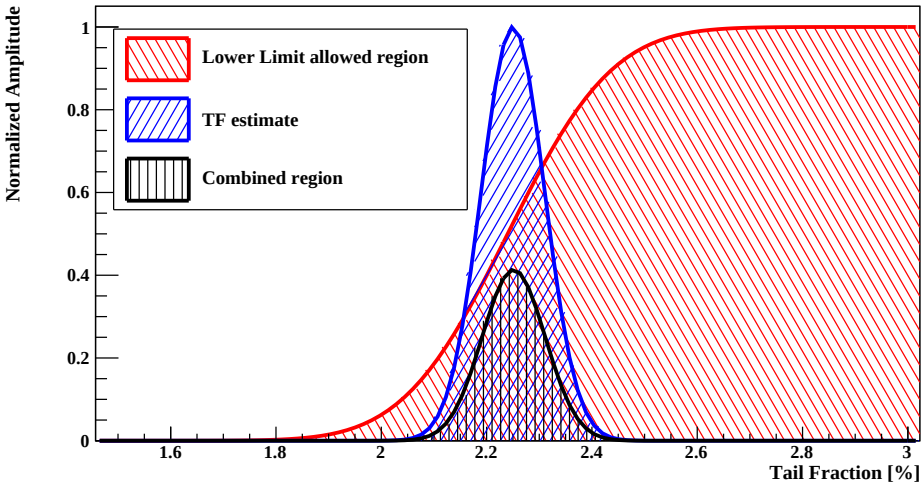

Figure 3.20: The allowed region for the tail fraction obtained from lineshape data, estimated by a Gaussian distribution is shown in blue. The region for the lower limit is obtained from the error function and indicated in red. The black shaded region represents the combined allowed region of the tail fraction.

We took the product of these two allowed regions to find the combined probability function of the tail fraction. The latter is shown in figure 3.20 in black. The

statistical analysis of the moments of this probability function served as a handle to find the mean and variance of the distribution. The first and second moment (μ_1 and μ_2) of a probability distribution within the interval [a,b] are defined as

$$\mu_1 = \int_a^b x \cdot f(x) dx \tag{3.11}$$

$$\mu_2 = \int_a^b x^2 \cdot f(x) dx \tag{3.12}$$

With these definitions, the mean $\bar{x}$ corresponds to the first moment μ_1 and the variance is defined as $\sigma^2 = \mu_2 - \mu^2$. Using the combined probability function of the tail fraction as f(x), we obtained the following result: [2]

$$TF = (2.25137 \pm 0.05996)\,\% \tag{3.13}$$

[2]More than the standard significant digits are printed to indicate the difference of the combined value from the tail fraction obtained from the lineshape measurement.

Chapter 4

Muon Capture Experiment

4.1 Introduction and Theoretical Background

The LHC offers a unique opportunity to search for new hypothetical particles. At the energy scale of heavy resonances, it is the most promising accelerator in the search of parity-violating processes. Nevertheless, weakly coupled particles with low mass might be missed at the high energies and luminosities present at the LHC. Therefore, complimentary experiments at low energies with high intensity are crucial in order to cover this part of the energy scale [13].

One of the puzzles brought to light by low energy experiments is the discrepancy in the charge radius of the proton r_p. It was recently measured to be $r_p = 0.84184(67)\,\text{fm}$ on a muon-proton system by determining the value from the muonic hydrogen Lamb shift [12]. The currently most accurate value from electron-proton systems, published by the CODATA compilation of physical constants, $r_p = 0.8768(69)\,\text{fm}$ [24], reveals a striking difference of five standard deviations compared to the measurement in the muon-proton system. This discrepancy could be due to missing elements within the SM or experimental mistakes, however it could also bring to light New Physics (NP).

Another unresolved issue concerns the anomalous magnetic moment of the muon α_μ. The theoretical calculation of this observable deviates from the value obtained by experiments; in the E821 experiment at Brookhaven National Laboratory the precession of μ^+ and μ^- in a constant external magnetic field was studied

while the muons were circulating in a storage ring. Combining their values into an average and assuming CPT invariance resulted in $\alpha_\mu^{exp} = 11659208.9(5.4)(3.3) \times 10^{-10}$, where the first error originates from statistics, the second one from systematic effects [11] [1]. The theoretical value on the other hand, is calculated to be $\alpha_\mu^{SM} = 116591802(2)(42)(26) \times 10^{-11}$ combining electroweak, hadronic, and QED contributions. e^+e^- data provides a value for the hadronic vacuum polarization and the errors in the quoted SM value are due to electroweak, lowest-order hadronic, and higher-order hadronic contributions [25]. The difference between theory and measurement of the muon anomalous magnetic moment is $3.6\,\sigma$.

As the two examples above illustrate, muon physics presents a field of interest when studying discrepancies between predictions by the SM and tests with experiments. Consequently, muons are well suited for studies probing new physics interactions and hypothetical particles. As discussed in reference [26], such physics beyond the SM might originate from a force carrier in the MeV energy range or lower, preferentially coupling to muons.

A new light vector mediator seems promising when comparing the hierarchy of r_p values obtained from atomic hydrogen and deuterium, e-p scattering and muonic hydrogen, and when considering the data on neutrino scattering in the low MeV energy range as well as neutrino oscillations [26]. If we divide the new interaction into couplings with left and right handed SM fermions, the left-handed fermion interaction can be excluded since it involves a neutrino field and we know from experimental data that no new interactions between neutrinos and electrons or nucleons occur at a level higher than the Fermi constant. This leaves only the right-handed fermion current. However, parity non-conservation tests in the electron sector exclude large neutral right-handed currents for electrons, therefore the most promising candidate is a vector particle coupling to right-handed muons [26].

Focusing on a new $U(1)_R$ gauge symmetry, this leads to parity-violating muon-proton neutral current interactions. McKeen and Pospelov consider a low-energy effective neutral current Lagrangian in reference [13] as follows:

[1] The latest value for the absolute muon-to-proton magnetic ratio was used to determine α_μ^{exp} as for citation in [25].

$$\mathscr{L} = \mathscr{L}_{SM} + \mathscr{L}_{NP} \tag{4.1}$$

$$\mathscr{L}_{SM} = -\frac{G_F}{2\sqrt{2}}\bar{\mu}\gamma_\nu\gamma_5\mu(g_n\bar{n}\gamma_\nu n + g_p\bar{p}\gamma_\nu p) \tag{4.2}$$

$$\mathscr{L}_{NP} = \bar{\mu}\gamma_\nu\gamma_5\mu\frac{4\pi\alpha g_\mu^{NP}}{m_V^2+\Box}\left(g_n^{NP}\bar{n}\gamma_\nu n + g_p^{NP}\bar{p}\gamma_\nu p\right) \tag{4.3}$$

Both SM and NP contributions are included in this Lagrangian, and the vector couplings to nucleons take the values $g_n = -\frac{1}{2}$, $g_p = \frac{1}{2} - 2\sin^2\theta_W$, where θ_W is the Weinberg angle; $\Box = \partial^\mu\partial_\mu$ is the d'Alembert operator. When studying this model, the most freedom in the parameter space corresponds to a mass of the mediator gauge boson of $m_V \simeq 30\,\mathrm{MeV}$. Assuming this value for m_V and fitting to the proton charge radius, the strength for the muon proton interactions is at the order of [13]

$$\frac{4\pi\alpha g_\mu^{NP} g_p^{NP}}{m_V^2} \simeq \frac{2\times10^{-5}}{(30\,\mathrm{MeV})^2} \gg G_F \tag{4.4}$$

A possible way to test the manifestation of equation 4.1 is to study the Atomic Radiative Capture (ARC) of μ^- into medium Z atoms. In particular, the direct radiative capture of a muon into the 2S state is of interest: $\mu^- + Z \to (\mu^- Z)_{2S} + \gamma$. The level diagram for a typical muonic atom is shown in figure 4.1. If we measure a non-zero expectation value of a pseudoscalar observable, we have an indication of a neutral current. Experimentally, this can be realized by measuring the angular distribution of photons emitted during the atomic transitions. The customary terminology to describe the state of the photons is as follows: the photon has a total angular momentum j, composed of the spin s and the orbital angular momentum l, which can take the values 1,2,3,.... For each value of j, two states exist distinguished by their parity of either $(-1)^j$ or $(-1)^{j+1}$. In the first case, the photon is called an electric 2^j-pole photon (E_j), in the second case it is called a magnetic 2^j-pole photon (M_j) [27]. The observable we can detect in an experiment is proportional to the ratio between the transition amplitudes of two states. Therefore, choosing a transition where the parity-allowed process is suppressed will increase

the chance to detect a parity-odd process. Due to the selection rule for the orbital angular momentum l, $\Delta l = \pm 1$, the parity-allowed transition from the 2S state to the 1S state via a magnetic dipole transition (M_1) is suppressed because of the orbital quantum number. However, the transition of the 2P state into the 1S state occurs via a normal electric dipole transition (E_1) with a change of $\Delta l = -1$. Consequently, the 2S state is preferred for an experiment with focus on observing a parity-odd process [28].

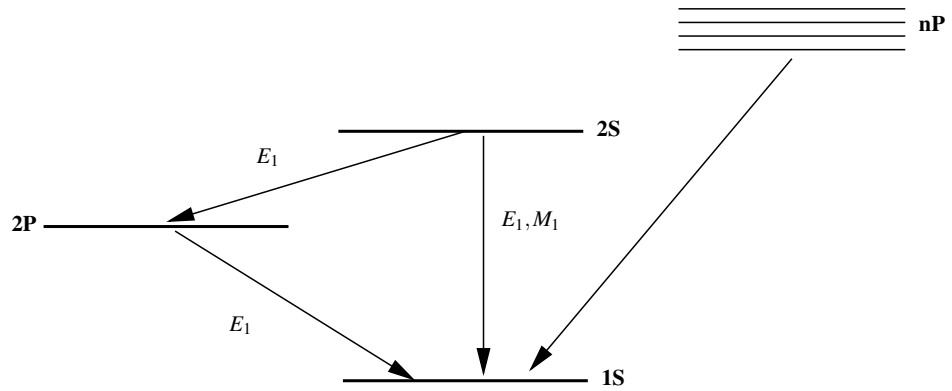

Figure 4.1: A level diagram of a typical muonic atom. Transitions between the 2S and 2P state to the 1S state are shown as well as those from higher levels (nP).

So far, the single photon transition from the 2S state to the 1S state has not been measured in any muonic atom. This is mostly due to the small branching ratio of the one photon decay of the 2S state in light elements and the fact that the 2P-1S transition is by far more dominant. In atoms with higher charge number ($Z \sim 30$) it is considerably easier to distinguish between the 2S-1S and 2P-1S transitions as the energy difference between the 2S and 2P states is substantially larger. However, there is a high background due to transitions from higher levels into the 1S state, the so called cascade process, which occurs for muons at rest. Therefore, the 2S-1S transition has not been observed until now in heavier atoms either [13].

Consequently, McKeen and Pospelov suggested an experimental setup to observe the 2S-1S transition which was slightly different from the ones used thus far. In contrast to previous attempts where the incoming muons were stopped completely, their approach was to use thin targets with $Z \geq 30$ in which the muons are

only slowed down, decreasing the probability for muonic cascade processes considerably. Some of the muons will be directly captured into the 2S state, emitting photons in two steps [13]:

$$\mu^-_{\rightarrow} + Z \Rightarrow (\mu^-_{\rightarrow} Z)_{2S_{1/2}} + \gamma_1 \tag{4.5}$$

$$2S_{1/2} \Rightarrow 1S_{1/2} + \gamma_2 \tag{4.6}$$

The notation $\mu^-_{\rightarrow}$ indicates a longitudinally polarized muon, γ_1 and γ_2 are the two emitted photons. The energy of γ_1 is the sum of the kinetic energy of the muon and the binding energy of the atom in the 2S state. The energy of γ_2 is approximately 2 MeV, and its angular distribution represents the expectation value of the pseudoscalar observable exhibiting parity violation [13].

The cross section of the ARC process into the 2S state is calculated analogously to electron-nucleus photorecombination, derived from the hydrogen-like photoelectric ionization cross section $\sigma^{(0)}_{PE}$, using a dipole approximation and assuming a point-like nucleus. With the dipole approximation, the probability of the transition from one state to a lower state with emission of a photon is estimated. The electrons are assumed to be non-relativistic and the interaction between the radiation field and the electron is estimated as a small perturbation. Furthermore, it is assumed that the electrons are at a distance from the nucleus at the order of the Bohr radius ($\sim 10^{-8}$ cm), so that the wave number of the emitted light (for visible light $\sim 10^5\,\mathrm{cm}^{-1}$) is considerably smaller than 10^{-8} cm. This leads to an expression of the matrix element similar to dipole radiation, hence the name of the approximation. The angular distribution of dipole radiation is proportional to $\sin^2(\theta)$ where θ is the angle between the dipole moment and the direction of observation [29]. When accounting for the finite nuclear charge radius and departing from the dipole approximation, the cross section takes the form [13]:

$$\sigma_{ARC} = \frac{2\omega^2}{p^2}\sigma_{PE} \tag{4.7}$$

$$\sigma_{PE} = \eta(p, R_c, Z, n, l) \times \sigma_{PE}^{(0)}(nl) \tag{4.8}$$

$$\sigma_{PE}^{(0)}(2S) = \frac{2^{14}\pi^2\alpha a^2 E_2^4}{3\omega^4}\left[1+\frac{3E_2}{\omega}\right]\frac{\exp\left(-\frac{4}{pa}\cot^{-1}\frac{1}{2pa}\right)}{1-\exp(-2\pi/pa)}, \tag{4.9}$$

where p represents the incoming muon momentum, E_2 is the binding energy of a muon in the 2S state, α is the Bohr radius, $\omega = p^2/2m_\mu + E_2$ is the energy of the photon emitted during the ARC process, $a = (Z\alpha m_\mu)^{-1}$ and n and l are the principal and orbital quantum number respectively. The factor in front of the photoelectric ionization cross section η is obtained by numerically solving the Schroedinger equation under the assumption that the muon is moving in the field of the nucleus which has a uniform charge distribution of radius R_c. The capture cross section decreases for increasing momentum, consequently relatively slow muons are required for an experiment with a high signal rate. However, at very low energies, the background process of a capture at rest dominates, so the trade off between signal and background has to be considered when choosing the muon momentum for an experiment.

The probability for the ARC process into the 2S state $P_{ARC,2S}$ depends on the initial and final momentum of the muons passing through the target, p_{min} and p_{max}, as well as the number density of the target material n as follows [13]:

$$P_{ARC,2S} = \int_{p_{min}}^{p_{max}} dp \frac{n \cdot \sigma_{ARC,2S}}{|dp/dx|}. \tag{4.10}$$

The emission rate $\frac{dN_{2S-1S}}{dt}$ of the next step involving the 2S-1S transition and emittance of the second photon γ_2 is estimated from the probability for the capture process (4.10), the muon flux Φ_{μ^-} and the branching ratio for single photons in the 2S state $\mathrm{Br}_{1\gamma}$ [13]:

$$\frac{dN_{2S-1S}}{dt} = P_{ARC} \times \mathrm{Br}_{1\gamma} \times \Phi_{\mu^-}, \tag{4.11}$$

$$\text{for Z} \sim 30, \mathrm{Br}_{1\gamma} \text{ is given by} \tag{4.12}$$

$$\mathrm{Br}_{1\gamma} \approx \frac{\Gamma_{2S-1S+1\gamma}}{\Gamma_{2S-2P}} \sim 2 \times 10^{-3}. \tag{4.13}$$

Given the specifics of an experimental setup concerning the target and muon flux, the emission rate of the two photons can be calculated.

4.2 Experimental Realization

The experimental realization of observing the ARC process described above requires a beam of polarized muons and an adequate detector system which can measure the energy of the emitted photons and their timing as well as their spatial distribution. The PIENU experiment at TRIUMF provided a high resolution calorimeter for the energy measurement and tracking detectors to characterize the beam and set up an appropriate trigger. In addition, the M13 beamline delivered not only pions, but also muons. However, these muons had a low level of polarization since they were mostly produced as cloud muons [30] near the production target. Therefore it was impossible to use polarized muons at TRIUMF with the current setup. In spite of that, the first part of the ARC process involving the emittance of the photon γ_1 could be realized with the existing equipment. This partial study is of high interest since the direct capture of a muon into the 1S or 2S state of an atom has not been observed yet. Therefore, we collected data in a special run in December 2012 in order to study this direct capture process.

For this run, we added a medium atomic number target in the detector system close to the NaI(Tl) crystal, which measured the energy of the emitted photon. A plastic scintillator in between the new target and the crystal served as veto counter to reject any events where charged particles were emitted from the target in order to select only neutral particles. The components of the PIENU detector are shown in figure 2.4. The cosmic ray trigger from the PIENU experiment vetoed cosmic ray

muons. Since a gaseous target involves a considerable amount of equipment and a complicated handling procedure, a metal foil was more suitable for the PIENU detector setup than the krypton target suggested in reference [13]. The charge number of zirconium $Z_{Zr} = 40$ is close to that of krypton $Z_{Kr} = 36$, which is why a zirconium foil was chosen as target.

The cross section of the radiative capture into the 1S state is approximately five times larger than that into the 2S state, so the main focus of the experiment was to detect photons emitted during the 1S capture. Figure 4.2 shows the ARC cross section into the 1S state of zirconium versus the muon momentum, as calculated by M. Pospelov and A. Fradette [31].

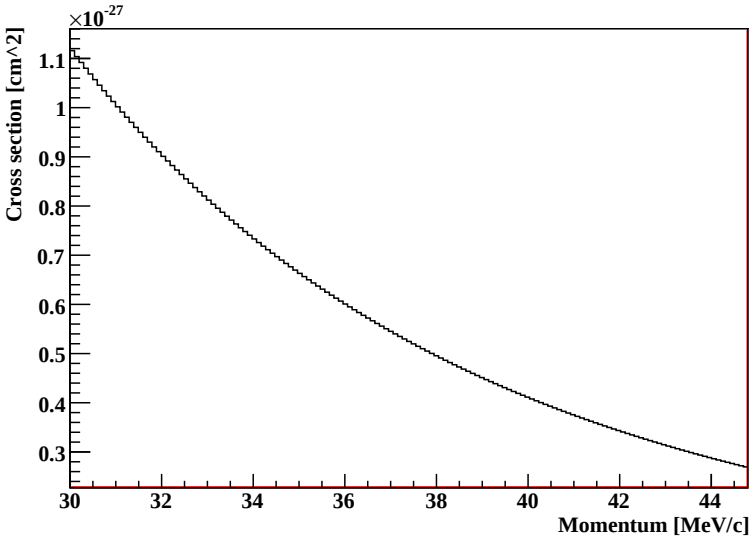

Figure 4.2: Cross section of ARC into the 1S state of zirconium versus muon momentum, calculated by M. Pospelov and A. Fradette.

By tuning the M13 beamline to negative muons and adjusting the momentum, all of the requirements for the direct capture process were met. The experimental procedure and data analysis are described in the following sections.

4.2.1 Beamline

A full GEANT4 simulation of the PIENU detector existed already, including a parameterized pion beam entering the first detector element and then simulating the tracks of particles through all of the different elements until they reached the calorimeters. This simulation was used in studies for the muon capture experiment. Changing the incoming particle beam from π^+ to μ^- allowed the study of a muon's energy deposit in the detector elements. This study showed that a Zr target was best placed in front of the third wire chamber (WC3) (see figure 2.4). With an incoming muon momentum of (72.0 ± 0.4) MeV/c, the particles were degraded to (37 ± 3) MeV/c when entering the new target, as shown in figure 4.3. At this low momentum the cross section for the direct capture process was larger than at higher momenta and most muons still had sufficient kinetic energy to traverse the target and potentially undergo the muon capture process followed by the cascade. With a higher beam momentum of (74.0 ± 0.4) MeV/c the muons' momentum decreased to (44 ± 2) MeV/c at the entrance to the Zr foil, as shown in figure 4.4. At this momentum, the probability for both a capture at rest and a direct radiative capture was smaller, resulting in less background but also a smaller signal cross section. We took data with both momentum settings, as discussed in section 4.2.4.

For the collection of data in December 2012, the fields of the bending magnets were reversed to guide negatively charged particles through the beamline instead of the positively charged particles used in the PIENU experiment. As described in section 2.2, a degrader was placed in the beam producing a spread between the different particle kinds after the second bending magnet. Therefore, the collimator after this magnet was placed in the correct position to select muons instead of pions. Furthermore, the strength of the magnetic fields in the quadrupoles and bending magnets was adjusted for a momentum of 72 MeV/c or 74 MeV/c respectively. By tuning the slits and absorbers, we focused the beam in the center of WC1 where it entered the detector.

4.2.2 Detector

The only modification to the PIENU detector system was the addition of a new target where the radiative capture took place. During the preparation of the ex-

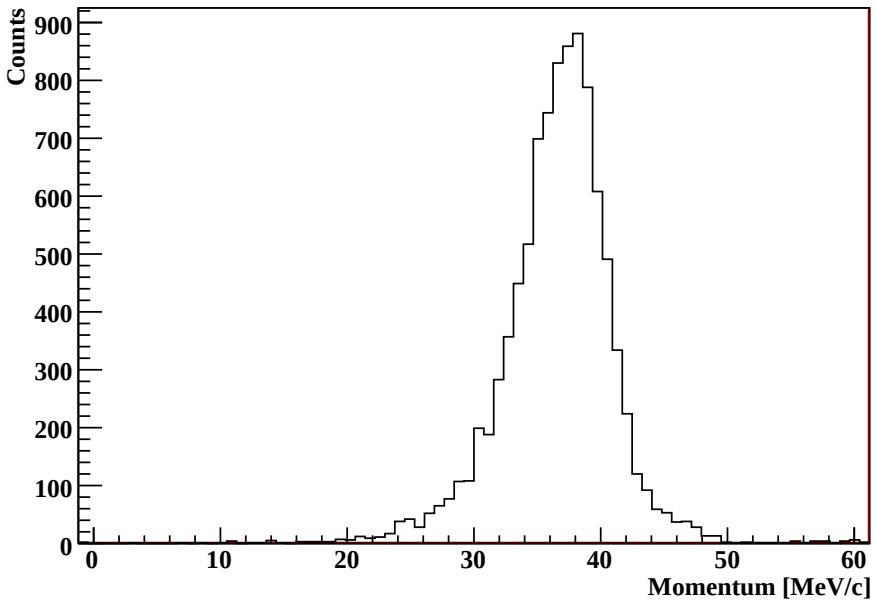

Figure 4.3: Momentum distribution of muons entering the Zr foil for a beam momentum of 72 MeV/c, obtained from the MC simulation.

periment and the studies with the GEANT4 detector simulation, several different materials for a possible target were studied. Comparing molybdenum (Z = 42), copper (Z = 29) and zirconium (Z = 40) showed that zirconium would best meet the requirements of momentum degradation with an acceptable spread in the momentum distribution. To determine the thickness, the momentum before and after the zirconium was obtained from the simulation. A thickness of 0.25 mm degraded the incoming 37 MeV/c muons by $\sim$ 3 MeV/c in momentum. A zirconium foil with this thickness was placed in front of WC3, as shown in figure 4.5. Figure 4.6 shows a photograph of the detector elements upstream of the third wire chamber with and without the zirconium foil.

4.2.3 Trigger

The type of event we were interested in was an incoming muon absorbed in the zirconium, where the radiative capture occurred and only a photon was emitted.

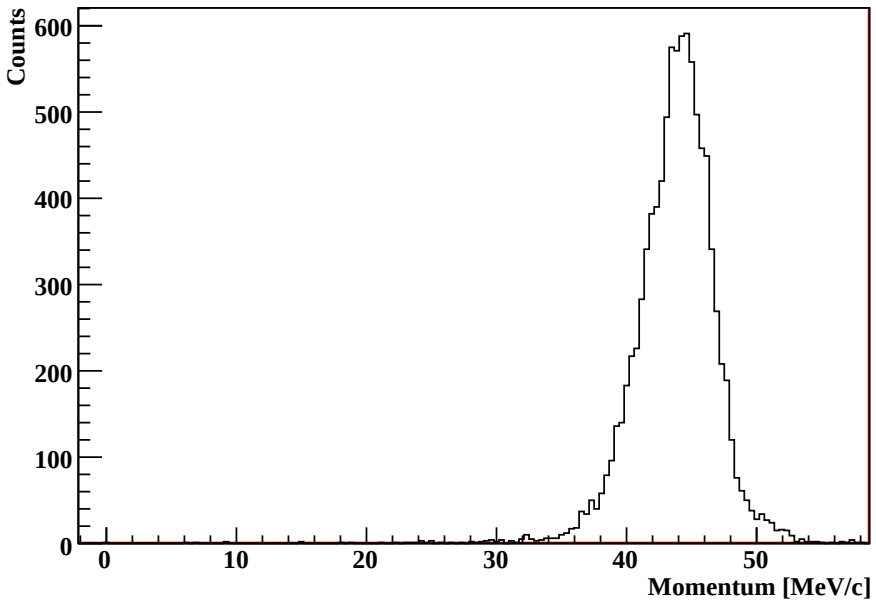

Figure 4.4: Momentum distribution of muons entering the Zr foil for a beam momentum of 74 MeV/c, obtained from the MC simulation.

Consequently, we required a charged particle to pass through all of the detector components in front of the zirconium, namely B1, B2, Tg and T1. In addition, we rejected any charged particles after the zirconium. The only counters present after the foil were T2 and WC3, so they both would be used as a veto counter. The special physics triggers for the PIENU experiment described in section 2.3 were turned off, only the electron and cosmics triggers were used in order to calibrate the scintillators and calorimeters for the data analysis and reject cosmic muon events.

4.2.4 Data Taking

While tuning the beam and monitoring the trigger rates in the various counters, we noticed that the majority of μ^- selected with our trigger condition stopped in front of the T2 counter when entering the detector system at 72 MeV/c. Most likely, this was due to the momentum spread and low energy tail of the muons (see figure 4.3). Since the stopping muons increased the chance of a muon capture at rest followed

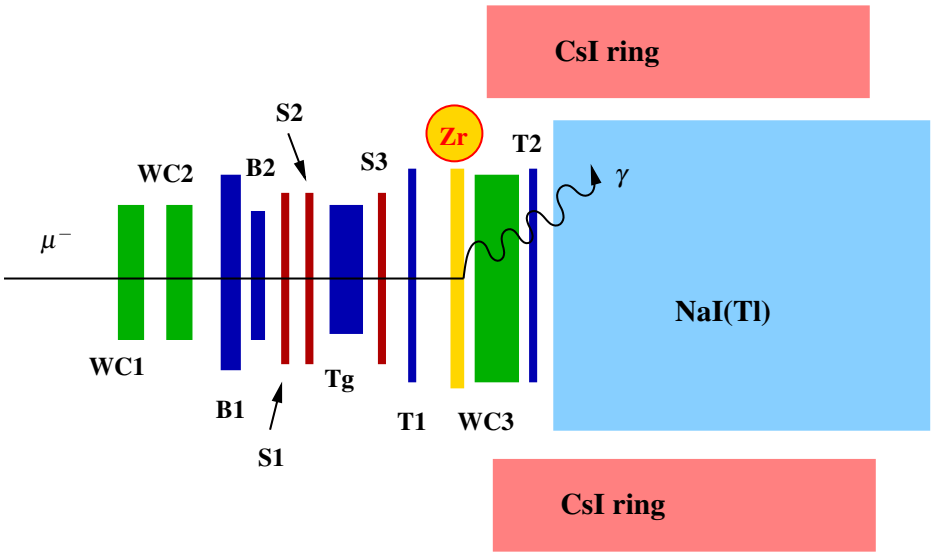

Figure 4.5: Diagram of the detector including the zirconium foil in front of the third wire chamber (WC3). (Schematic drawing, not to scale)

by the cascade process and therefore enhanced the amount of background, we took data in this condition for only 22 h, with a muon rate of 8.4×10^3 Hz. A second set of data was taken at 74 MeV/c for 16 h with a muon rate of 6.8×10^3 Hz and significantly fewer muons stopped in the zirconium target. Nevertheless, this was a trade-off between a high background rate and a high cross section of the radiative capture process since the latter increases with lower momentum, as shown in figure 4.2.

The simulation studies had shown that 0.71 mm of Mylar degrades the momentum by the same amount as 0.25 mm of zirconium. Mylar was therefore used to take background data. For 22 h a Mylar foil was placed in front of WC3 instead of the zirconium and we took data with a 74 MeV/c beam.

4.3 Data Analysis

The signal we were aiming to detect was a gamma ray originating from the direct radiative capture. Its energy spectrum in the NaI(Tl) crystal was simulated with GEANT4 to gain knowledge about what to expect within the data. In order to

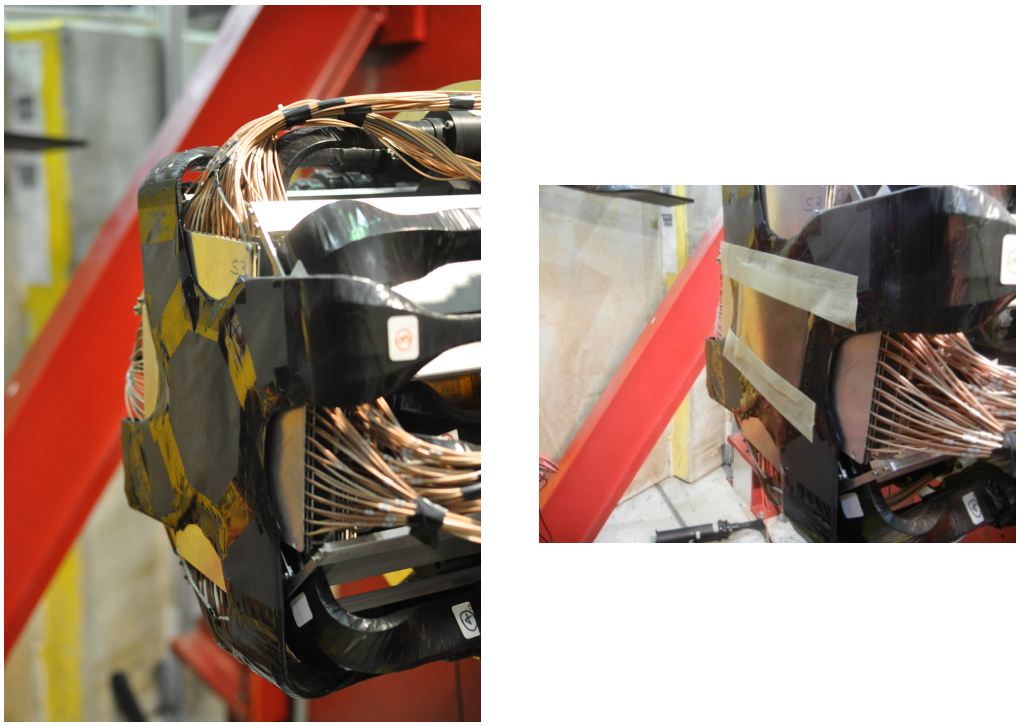

Figure 4.6: Detector parts downstream of the scintillator counter T1 which is the outermost component seen in the picture. The left panel shows the detector without the zirconium, the right panel shows the zirconium foil attached to T1.

extract the capture photons, the first requirement was to calibrate the energy output from the NaI(Tl) crystal. After that, selection cuts were applied to suppress the background mostly due to the muon capture at rest. Since the largest difference between the radiative capture and the capture at rest is their timing, sufficient time resolution from the NaI(Tl) was necessary. Furthermore, neutrons originating from the background process had to be identified and suppressed.

To avoid bias, a blind analysis was performed and the background was predicted from the blinded energy spectrum. Comparing the background to the simulation of the signal process assessed whether or not the signal would be detectable.

Finally, a procedure to extract the signal from the background was developed and steps to take after the unblinding were planned. The following sections describe the procedure of data analysis.

4.3.1 Simulation of the Signal

We obtain the energy of the ARC photon by summing up the muonic binding energy of the excited state and the kinetic energy of the muon. For zirconium, the muonic binding energies of the 1S and 2S states are the following [32]:

$$E_{1S} = 3643\,\text{keV} \tag{4.14}$$

$$E_{2S} = 1021\,\text{keV} \tag{4.15}$$

Due to the larger cross section of the 1S state, we focused on the signal produced by the capture into this state only. The kinetic energy of the muons was determined from the GEANT4 simulation. Figures 4.3 and 4.4 show the momentum distributions for muons entering the zirconium foil at the two different settings. Due to the width of the distributions and the energy loss within the foil, the cross section of the ARC capture varied within the zirconium. To account for this, the zirconium foil was segmented into five slices in the beam direction. In a simulation with muons entering the detector at the two different momentum settings, the kinetic energy distributions for each of the slices were determined. Based on these and the 1S binding energy, the energy distributions for emitted photons were calculated. In a second simulation, photons departing from within each of the slices according to the determined energy distribution were simulated. The azimuthal angle had a flat distribution between zero and 2π, whereas the distribution of the photons' polar angle was obtained from the cross section calculated by M. Pospelov and A. Fradette and is shown in figure 4.7 for both momentum sets. The distribution can be explained by the fact that not only the electric dipole transition E_1 contributes to the cross section, but also higher order transitions are taken into account. When only considering E_1, the distribution of the polar angle is proportional to $\sin^3(\theta)$, which is similar to the electric dipole radiation mentioned in section 4.1. However, as the photon is traveling with momentum p, also transverse components of other

wave functions contribute and the angular distribution departs from the $\sin^3(\theta)$ dependence and is a function of the momentum. Consequently, the polar angle distribution shown in figure 4.7 takes a slightly different shape for the two momentum settings.

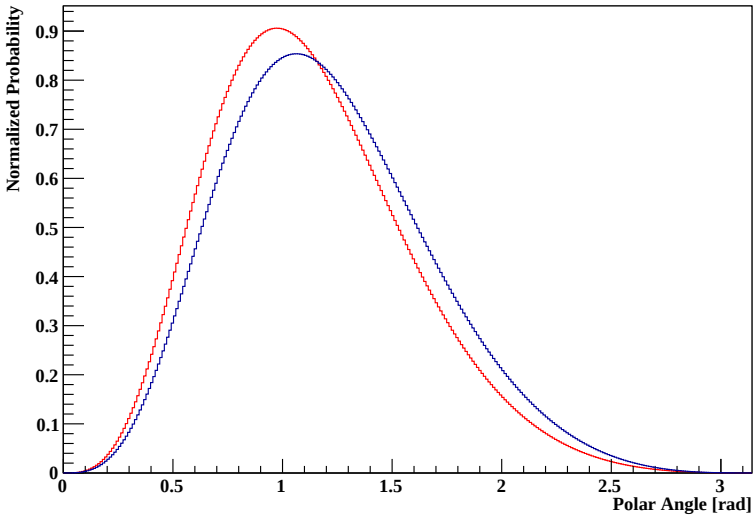

Figure 4.7: Probability of the ARC photon being emitted at a certain polar angle. The red line is for the 74 MeV/c momentum set, the blue line for the 72 MeV/c set.

From the photon simulation, the energy deposit in the NaI(Tl) crystal was extracted for events with no hit in the T2 counter. It is shown for the five different slices in the left panel of figure 4.8 for the 72 MeV/c momentum set. These five energy distributions were then added together, weighted by their respective cross sections and the resulting energy distribution is shown in the right panel of figure 4.8. Figure 4.9 shows the energy slices as well as the total signal energy in the NaI(Tl) for the 74 MeV/c momentum set. Based on the results from the simulation, the signal energies from the 1S state expected for the two momentum sets are summarized in table 4.2.

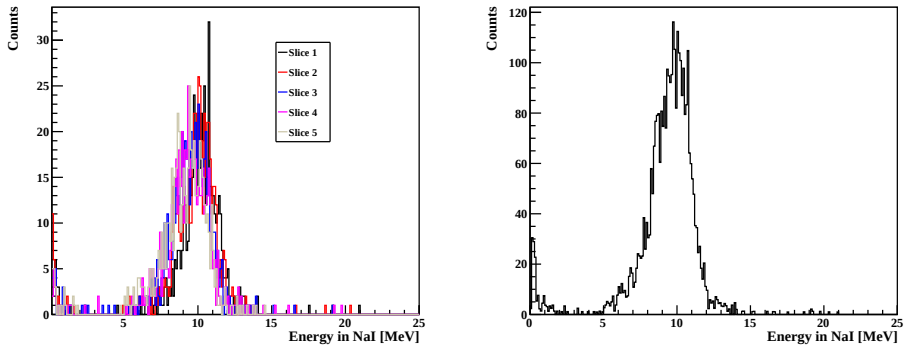

Figure 4.8: Left Panel: The kinetic energy of the muons in the five slices of the Zr foil for the 72 MeV/c momentum set. Right panel: All slices added together, weighted by their cross section.

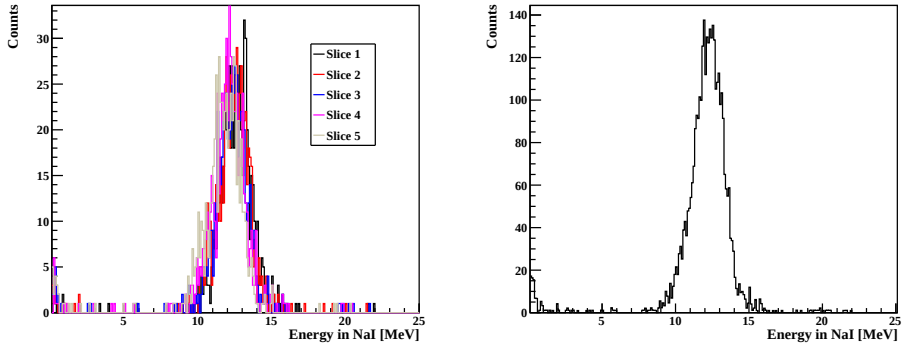

Figure 4.9: Left Panel: The kinetic energy of the muons in the five slices of the Zr foil for the 74 MeV/c momentum set. Right panel: All slices added together, weighted by their cross section.

4.3.2 Energy Calibration

The data from the electron trigger was used for calibration purposes. This trigger selected beam electrons which entered the NaI(Tl) crystal with an energy corresponding to the beam energy minus the deposit in the detector components before the crystal. The spectrum from the data was compared to a simulation of e^- passing through the PIENU detector including the zirconium foil. For comparison of

	72 MeV/c beam	74 MeV/c beam
1S state	9.7 ± 1.1 MeV	12.3 ± 1 MeV

Table 4.1: Signal photon energies for the two beam momenta for the 1S state.

the two spectra, they were both fitted to the Crystal Ball function, which combines a Gaussian with an exponential function as follows:

$$f(x;\alpha,n,\bar{x},\sigma) = N \cdot \begin{cases} \exp\left(-\frac{(x-\bar{x})^2}{2\sigma^2}\right), & \text{for} \quad \frac{x-\bar{x}}{\sigma} > -\alpha \\ A \cdot \left(B - \frac{x-\bar{x}}{\sigma}\right)^{-n}, & \text{for} \quad \frac{x-\bar{x}}{\sigma} \leq -\alpha \end{cases} \tag{4.16}$$

$$A = \left(\frac{n}{|\alpha|}\right)^n \cdot \exp\left(-\frac{|\alpha|^2}{2}\right) \tag{4.17}$$

$$B = \frac{n}{|\alpha|} - |\alpha| \tag{4.18}$$

N is a normalization constant, $\bar{x}$ corresponds to the mean of the Gaussian part and σ represents its width. The variables α and n describe the ratio of the exponential part to the Gaussian portion and the decay constant of the exponential.

By comparing the mean values obtained from the fit, the optimum calibration factor was determined. Figure 4.10 shows the energy spectra from MC and the data with the fit after the calibration procedure for the 72 MeV/c data set. The mean value determined from the fit is $\sigma = 65.8\,\mathrm{MeV/c}$ for both spectra, so the data is correctly calibrated. The same procedure was repeated for the 74 MeV/c data set to identify its calibration factor.

4.3.3 Selection Cuts

After calibrating the data, we applied a number of selection cuts ensuring that only events with one incoming muon were considered that did not reach the counter T2. First, events triggered by one of the calibration triggers were rejected to reduce the contamination of electrons. Then, a pile up cut was applied requiring one hit only in the upstream counters B1, B2, Tg and T1 as well as no hits in these counters before the incoming particle caused the trigger. In addition, no hits were allowed

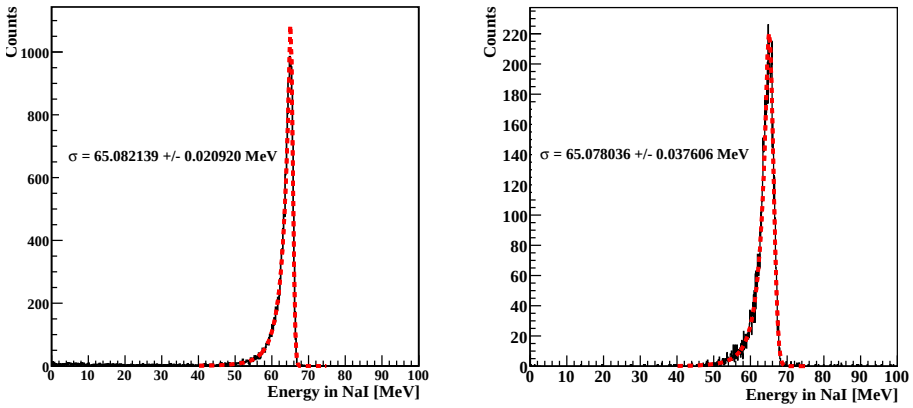

Figure 4.10: The comparison of a 72 MeV/c e^- beam in the detector simulation (left panel) with the calibrated electron triggered data (right panel) is shown in black. The red dashed line is a fit to a Crystal Ball function which results in a mean of $\sigma = 65.8\,\mathrm{MeV/c}$ in both cases.

in WC3 or the T2 counter, and only one hit was allowed in the NaI(Tl) crystal since the signal only contains one photon. These cuts ensured that one particle traversed the detector up to the counter T1 and no charged particle was detected after it, but one hit in the NaI(Tl) crystal was measured. The condition of only one hit in the NaI(Tl) might have killed potenial events where the muon underwent the ARC process into the 1S state and was subsequently captured by the zirconium. This case remains for further studies.

Furthermore, the incoming particle could be identified by its energy deposit in the upstream counters and the TOF with respect to the cyclotron RF timing. Figure 4.11 shows the charge collected by one PMT of the B1 counter versus the TOF for the 72 MeV/c data set. The three most populated areas in the plot correspond to π^-, e^- and μ^- particles. The energy loss per length is the largest for pions, so they correspond to the left area with the highest charge deposit, electrons deposit the least energy and muons range in between the two. Therefore, the mostly populated area to the far right corresponds to the muons within the beam. It was selected by a cut on the charge $130 < Q < 330$ (ADC channels) and the TOF $25 < t_{TOF} < 32$ (ns) as indicated by the red box in figure 4.11. Similarly, the charge deposit of

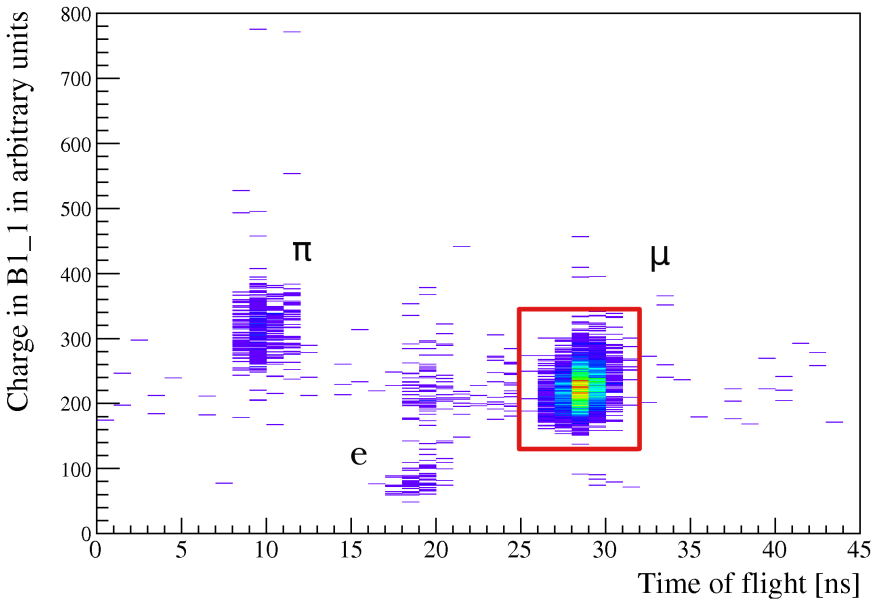

Figure 4.11: Charge collected by one PMT of the B1 counter versus the TOF with respect to the cyclotron RF timing. The red box indicates the cuts selecting muons.

μ^- for the other PMTs and the remaining counters was determined and cuts were placed accordingly. Analogously, the selection cuts for the 74 MeV/c data set were placed.

4.3.4 Background from Muon Capture At Rest

After selecting events with the signature of the ARC process, events resembling this process but originating from backgrounds had to be suppressed. The dominating background process was the muon capture at rest into a higher excited state which is followed by the cascade into the 1S state and the capture of the μ^- into the nucleus:

$$\mu^- + N(A,Z) \rightarrow \nu_\mu + N(A,Z-1) \tag{4.19}$$

When the muon is captured in the nucleus, the muon and a proton combine to form a neutron and a muon neutrino, reducing the proton number Z of the nucleus by one. Usually, photons, neutrons, and charged particles (protons) are also produced during this capture process [33]. The photons are emitted during the lower levels of the cascade process or originate from radiative muon decay. They could either reach the NaI(Tl) or undergo the photo-electric effect, pair-production or Compton scattering producing electrons which were rejected by the trigger condition. The low energy protons most likely did not exit the zirconium foil due to their high energy loss rate and would also have been vetoed by the trigger. The neutrons are caused by direct or evaporative processes, their energy ranges from very low energies to some 50 MeV. However, their emission after a muon capture is not very well understood and described by theoretical models yet and data is only available for a limited number of materials [33]. One theoretical model predicts resonance states analogously to photonuclear giant-resonance states, and broad energy peaks at low energies are also observed within data from muon capture in ^{12}C and ^{16}O [34]. The multiplicity of neutrons emitted in one capture process ranges from zero to three neutrons [33]. In the ARC experiment, any charged particles were rejected by the trigger and selection cuts; neutrons and photons however remained. Therefore, this background was reduced by distinguishing photons from neutrons using the pulse shape in the NaI(Tl) and by selecting photons only (see section 4.3.7).

The lifetime of the capture at rest in zirconium has been measured to be $\tau = (110 \pm 1)$ ns [35], so it could be further suppressed by applying a time cut since the ARC process occurs promptly.

4.3.5 Time Resolution

Since the timing was important to reduce the background detailed in the section above (4.3.4), it was crucial to have a good time resolution in order to place a cut directly around the prompt time. Data from the PIENU experiment was used to study the time resolution. First, the online sum of all the NaI(Tl) PMTs read out by the 500 MHz digitizer mentioned in section 2.3 was analyzed. An algorithm identifying hits in the pulseshape of the PMTs attributed a time to each hit within the crystal, and the time spectrum of the first hit was studied in this first study.

Events within the Michel spectrum were selected by requiring the prescaled trigger (see section 2.3) and a decay time $t > 100\,\text{ns}$. Since these decays range between 0 MeV and 50 MeV, they offered a good data sample for a wide range of energies including the signal region of interest. For slices of 2 MeV each, the time of the decay positron was determined and a Gaussian was fitted to the time distribution for this energy selection. The mean of the Gaussian corresponds to the positron time, its width represents the resolution at that particular energy. The resolution versus energy is plotted in figure 4.12 in the left panel, whereas the right panel shows the positron time. The time resolution around 10 MeV was $\sim 18\,\text{ns}$.

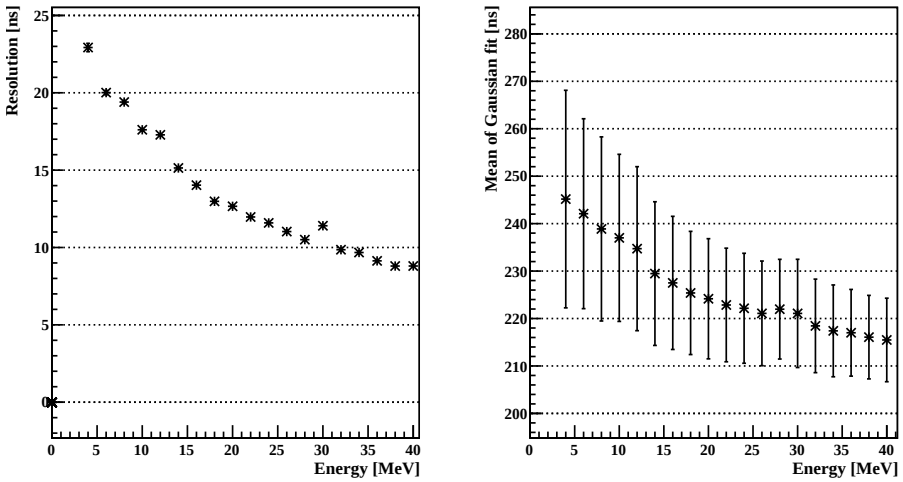

Figure 4.12: Time resolution (left panel) and positron time (right panel) determined from the hit finding algorithm for the 500 MHz digitizer. The uncertainty on the resolution is obtained from the error of the Gaussian fit and the error bars are very small. The width of the Gaussian distribution was used as estimate for the uncertainty of its mean.

In a second study, a different time variable was studied with respect to its resolution. As mentioned in section 3.1, a fit to the waveform was applied to the PIENU data based on a template. The input for this fit was the waveform from the 60 MHz digitizer for the online sum of the PMTs. Studying its resolution with the same method described above resulted in a time resolution of $\sim 16\,\text{ns}$ at the energy

region of interest. This was an improvement of 2 ns compared to the resolution of the time determined from the hit finding algorithm of the 500 MHz digitizer. Since the muon capture at rest process follows an exponential decay with a lifetime of 110 ns, $\sim 24\,\%$ of the decays have occurred after 16 ns. Consequently, for more background suppression, a better time resolution was needed to further restrict the region of the prompt time.

That is why a different fitting procedure was developed for the waveform in the NaI(Tl) crystal. It is not based on a template but on a fit to the Crystal Ball function, defined in equation 4.16. This fitting function was applied to the sum of the PMTs read out by the 500 MHz digitizer, which is the same waveform used in the first study. An example of such a waveform is shown in figure 4.13, also shown is the fit to the Crystal Ball function. The mean of the Gaussian part of the Crystal Ball function, $\bar{x}$, was used as definition for the pulse timing.

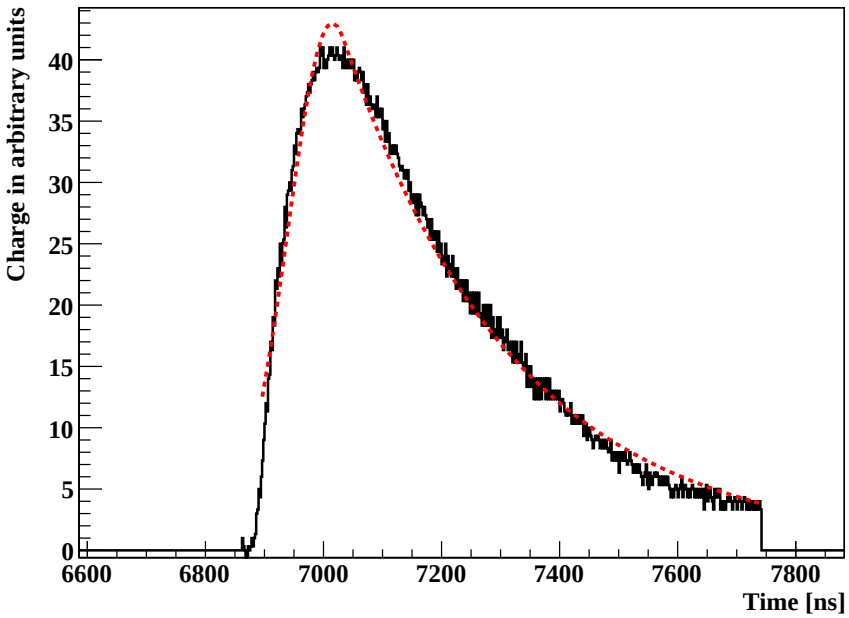

Figure 4.13: Waveform produced by a particle in the NaI(Tl) crystal (solid black line) shown with a fit to the Crystal Ball function (dashed red line).

This fitting procedure was used on the $\pi \to \mu \to e$ data set mentioned above for the resolution study which was performed similarly for the new fit. Figure 4.14 shows the time resolution versus energy when using the Crystal Ball function fit. For this fitting routine, the time resolution in the signal energy region was ~ 4 ns, which is an improvement of a factor of four compared to the previous fit and the lower digitization frequency. Therefore, this new procedure was used to analyze the muon capture data and to place a tight time cut around the prompt as described later in section 4.3.9. The prompt time varied within the resolution of ~ 2 ns around 20 MeV and was quite stable at the region of interest around 10 MeV.

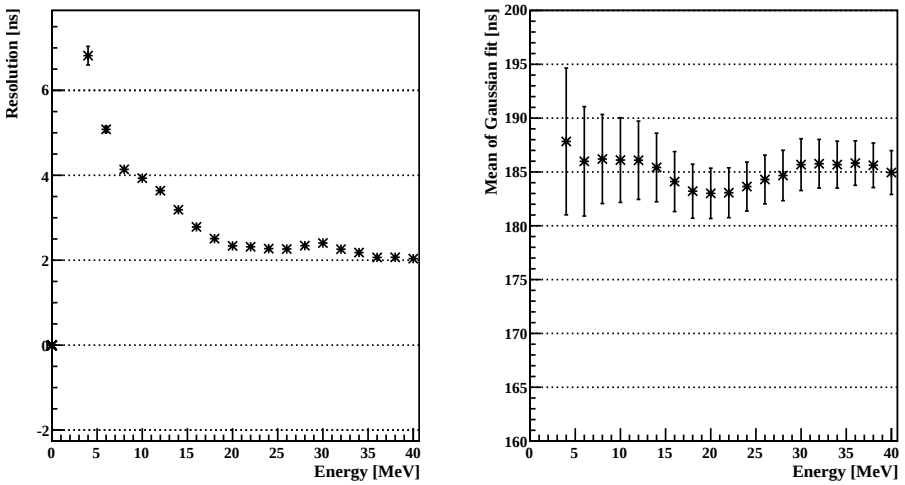

Figure 4.14: Time resolution versus energy for Crystal Ball function fit (left panel) and positron time determined from the mean of the Gaussian (right panel). As in figure 4.12, the uncertainty on the resolution is obtained from the error of the Gaussian fit and the error bars are very small. The width of the Gaussian distribution was used as estimate for the uncertainty of its mean.

4.3.6 Blind Analysis

For the remaining analysis, we applied a blinding technique to minimize bias. The signal region was concealed at the expected energy, taking into account a spread of

one σ and adding an additional 2 MeV region to both the lower and upper border. After this blinding, we could study the whole time spectrum and investigate the energy regions above and below the expected signal. In addition, we analyzed the data by blinding the prompt region in a window of 12 ns, corresponding to three σ for a time resolution of 4 ns at 10 MeV. With this blinding, we could study the whole energy region without the prompt photons from the ARC process. In the following sections, these two differently blinded data sets will be referred to as "energy-blinded" and "prompt-blinded" respectively.

First, we focused on the 72 MeV/c momentum set since we expected more background events at this lower kinetic energy. Consequently, the energy and time spectrum due to the background muon capture process could be studied. The low momentum data set was blinded between 6.6 MeV and 12.8 MeV.

4.3.7 Particle Identification

As mentioned in section 4.3.4, some of the particles emitted by the background muon capture process are neutrons. Since they are neutral they have the same signature as photons in the trigger. However, their waveform in the scintillator has a different shape. When interacting with the crystal atoms, the neutrons mostly knock out protons, which means that the waveform is characterized by the energy loss of a proton in NaI(Tl). Photons on the other hand, mostly interact via the photoelectric effect, Compton scattering and pair production, therefore producing electrons [36]. The scintillation process for these two particles differs slightly in NaI(Tl). In inorganic crystals, scintillation light is mostly produced by the activator impurities added to the crystal by doping. The energy deposit of a particle either produces electron hole pairs resulting in holes traveling in the valence band and electrons moving freely in the conduction band, or creates an exciton. This is a bound state of an electron and a hole, traveling through the so-called exciton band which is located slightly lower than the conduction band in the band structure of the crystal. After moving for some time, an electron and a hole are trapped in a doping center, or at a lattice defect or impurity, located between the valence and the conduction band, therefore exciting the center and emitting scintillation light during the de-excitation. If excitons were produced, they recombine after

some time when reaching a trap and also emit scintillation light. An explanation of the different behaviour for neutrons, protons and alpha particles versus that of electrons and photons can be found in reference [37]. The assumption is that either the time scale for electron-hole recombination or the diffusion to the activator centers is quite long when caused by electrons since their energy loss per distance dE/dx is small. Heavier particles on the other hand deposit considerably more energy, therefore the ionization density is higher and free particles are trapped more quickly. The scintillation pulse is characterized by a quick rise time of $\sim 60\,\text{ns}$ and a slow decrease with a decay constant of $\sim 230\,\text{ns}$ for both particle types. However, a pulse caused by an electron remains flat after initiation for about 150 ns due to the longer time-scale of recombination or diffusion [37]. Therefore, the pulse shape due to an electron or photon has a larger amplitude at late times compared to that caused by an alpha particle, a neutron, or a proton. Consequently, the waveform represents a handle to distinguish between different particle types. Pulse shape discrimination was successfully applied to distinguish between photons and neutrons in a NaI(Tl) crystal by P. Doll et.al [38] and for discrimination between alphas, deuterons, protons, and alphas and muons by G.H. Share [39].

We used a similar method to study the shape of the waveforms in the NaI(Tl) crystal of the PIENU detector. The parameter σ, extracted by the fitting procedure outlined in the section above (4.3.5), provides an estimate of the width of the main peak. We used it to define a tail region, as shown in figure 4.15. Since some wave forms from high energy pulses extended beyond the time window of the detector and their tail was truncated, we also defined the main pulse region in terms of its width to obtain a scalable definition of the main pulse. The integration limits are defined with respect to the mean $\bar{x}$ as follows:

$$\text{Lower integration limit for total integral:} \quad \bar{x} - 1 \cdot \sigma \tag{4.20}$$

$$\text{Lower integration limit for tail integral:} \quad \bar{x} + 2 \cdot \sigma \tag{4.21}$$

$$\text{Upper integration limit for both integrals:} \quad \bar{x} + 5 \cdot \sigma \tag{4.22}$$

First, the selection of Michel events from the PIENU experiment used for the time resolution study was analyzed with respect to the waveform shape. The in-

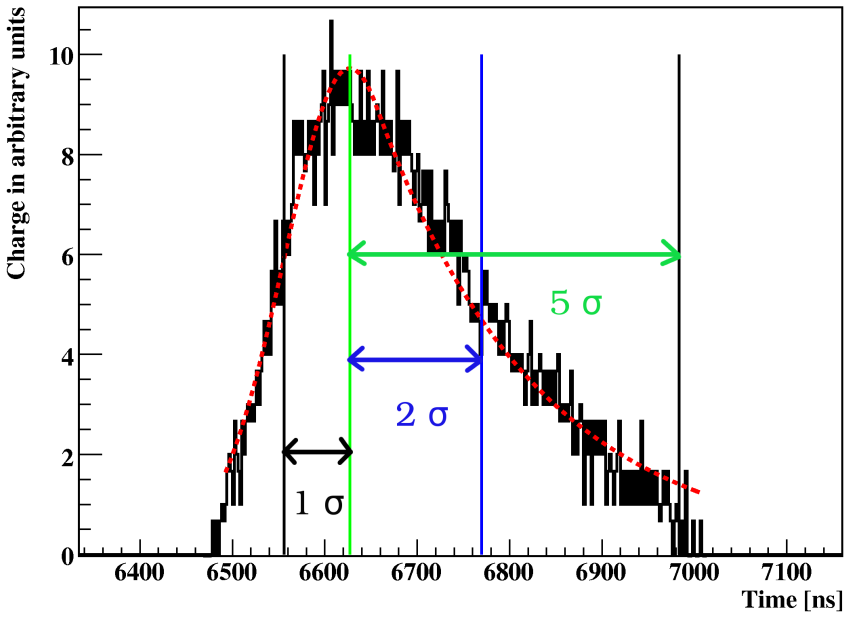

Figure 4.15: Waveform produced by a particle in the NaI(Tl) crystal (solid black line), with a fit to the Crystal Ball function (dashed red line). The vertical green line indicates the mean of the Gaussian, the vertical black line at one σ from the mean is the lower integration limit for the total waveform. The vertical blue line two σ to the right of the mean is the lower integration limit of the tail. Five σ away from the mean, indicated by the black line, is the upper integration limit.

tegral of the tail region versus the total integral is plotted in figure 4.16. We only expected photons and electrons after $\mu^- \rightarrow e\nu_\mu\nu_e$ decay. Since photons deposit their energy by interactions emitting electrons, the light in the scintillator was only produced by one particle kind which is confirmed by the fact that we only see one band in figure 4.16.

In a second step, we analyzed the 72 MeV/c prompt-blinded muon capture data set. Its tail versus total integral is shown in figure 4.17. The appearance of a second band compared to figure 4.16 suggests that there was a second type of particles producing scintillation light. Most likely, these originated from the neutrons from

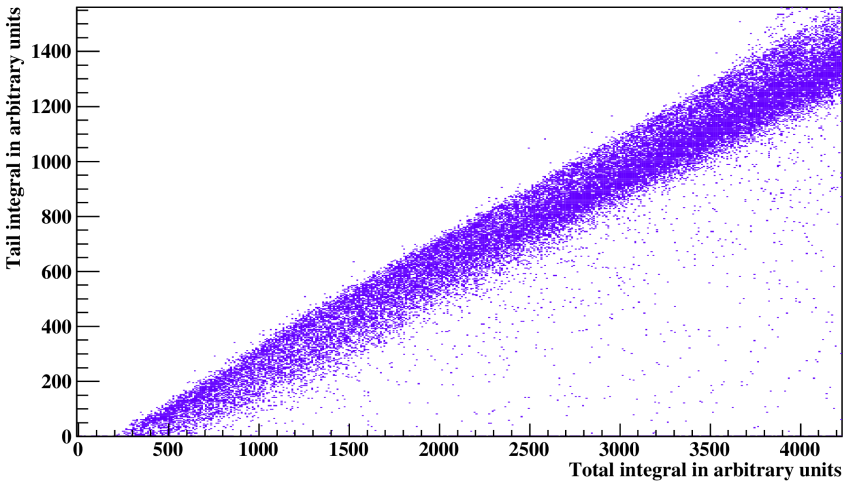

Figure 4.16: Integral of the tail region versus total integral of the waveform for PIENU data.

the muon capture background.

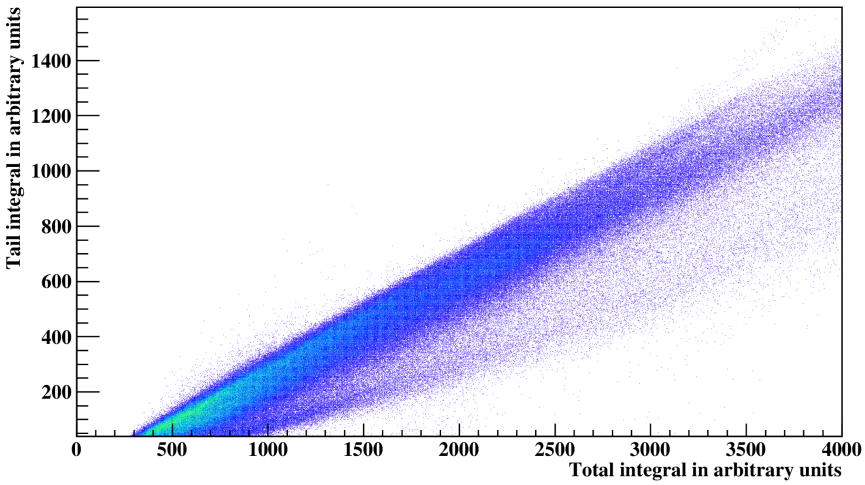

Figure 4.17: Integral of the tail region versus total integral of the waveform for muon capture data (72 MeV/c data set).

4.3.8 Rejection of Neutrons

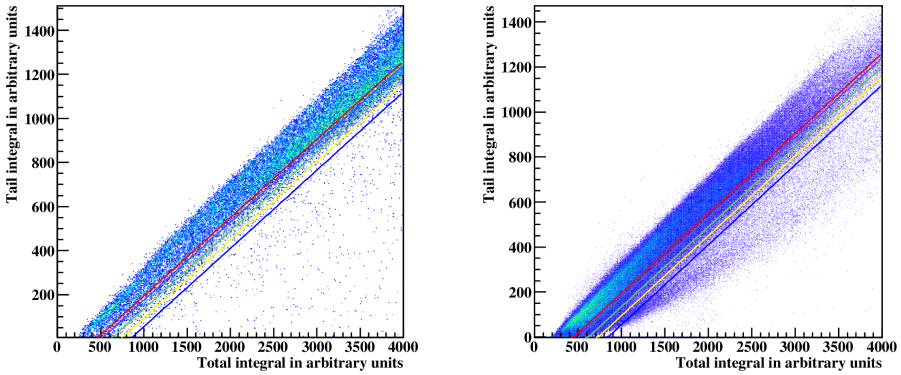

Figure 4.18: Integral of the tail region versus total integral of the waveform for PIENU data (left panel) and muon capture data (right panel) with various cuts indicated by the colored lines.

To suppress background events with neutrons, we made use of their different pulse shape in the NaI(Tl), compared to that of photons. Due to the difference between figures 4.16 and 4.17 we placed a straight line cut in between the photon and the neutron band. The PIENU data set provided us with a sample of electrons and photons, so this could be used as reference to decide which wave forms to accept. Various different selections are shown in figure 4.18 for both the PIENU data and the muon capture data. In order to determine which one rejected the most neutrons while preserving a sufficient amount of photons, the effect on the acceptance within the PIENU data set and on the rejection in both data sets were studied for the signal region in a one σ interval: $\Delta E_{Signal} = 8.6 - 10.8\,\mathrm{MeV}$. The acceptance A was defined as the number of events after applying a selection cut, divided by the number of events in the same region before any selection. Similarly, the rejection R was the number of events without applying a selection cut minus the number of events after applying the cut, normalized to the number of events without a selection. In figure 4.19 the rejection in the muon capture data minus the rejection in the PIENU data is shown for various cuts. Since any additional rejection in the muon capture data removes more events in the neutron band, the highest value for

the difference between the two indicates the highest neutron rejection efficiency. In figure 4.19 the cut with the highest efficiency is marked by a red square, and is labelled by number “8”. Figure 4.20 shows the acceptance versus rejection for the same cuts. Again, cut number “8” is indicated by a red square. The acceptance within the PIENU data set for this cut is 84 % and it is chosen as optimum cut for the remaining steps of the analysis.

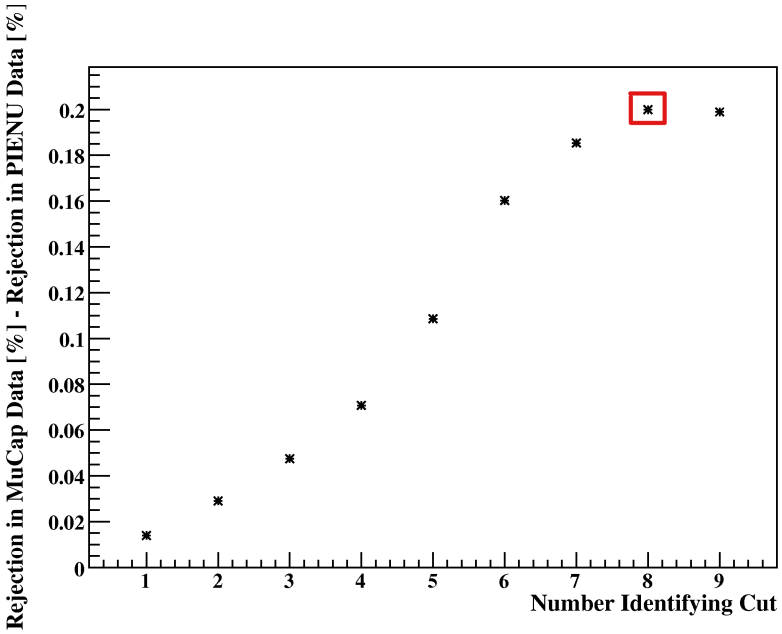

Figure 4.19: Neutron suppression efficiency, defined as the rejection in the muon capture data minus the rejection in the PIENU data, plotted for various cuts. The red square indicates the cut with the highest neutron suppression efficiency.

4.3.9 Time Cut

Finally, the last cut applied to the muon capture data was a time cut selecting the prompt region. Before the prompt time at 186 ns, a region of three σ of the Gaussian prompt peak was accepted in order to include a large portion of prompt events, but reject any random hits before the prompt time. After the prompt time, a tight cut at one σ was chosen in order to considerably reduce events originating from

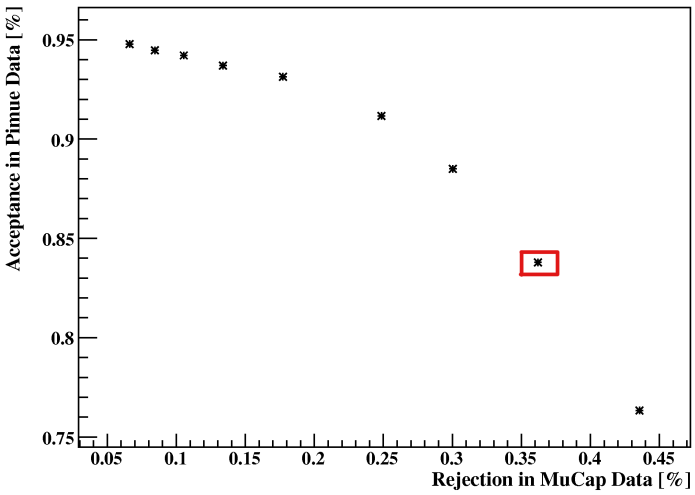

Figure 4.20: Acceptance (within PIENU data) versus rejection (within prompt-blinded muon capture data) for the same cuts used in figure 4.19. The red square indicates the same cut as the one in figure 4.19.

the muon capture cascade process with its long lifetime of 110 ns. However, this only cut out 15 % of the events in the prompt Gaussian, therefore accepting 85 % of them.

4.3.10 Analysis of the 74 MeV/c Data Set

The analysis of the 74 MeV/c data followed the same procedure as that for the 72 MeV/c data set. The energy-blinding was applied between 9.3 MeV and 15.3 MeV whereas the prompt-blinding was the same as for the 72 MeV/c data. The tail versus total integral of the pulse shape for the prompt-blinded data is shown in figure 4.21. At the higher momentum, fewer events were registered in total, so we had fewer statistics for this momentum set, but the two bands due to neutrons and photons are recognizable similarly as in the 72 MeV/c data. After studying the acceptance and rejection for several cuts on the waveform, the one with the highest neutron rejection efficiency was chosen again and then the same prompt cut as for the 72 MeV/c data set was applied.

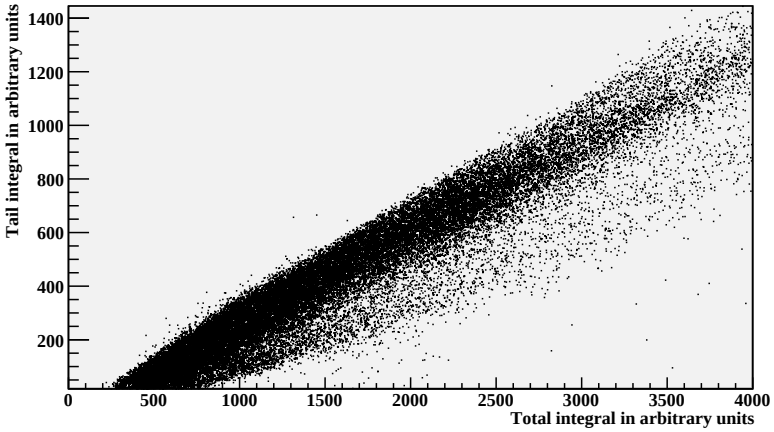

Figure 4.21: Tail versus total integral for the 74 MeV/c data set. Note that a different plotting style was used for this plot compared to the 72 MeV/c pulse shape plots due to the low statistics.

4.3.11 Analysis of the Mylar Data Set

The data taken with a Mylar foil instead of the zirconium foil was intended for background studies. As it was taken at the higher momentum of 74 MeV/c, the number of events stopping in the foil was not very high, so the statistics for this run are low. Figure 4.22 shows the integral of the tail versus the total integral of the waveform in the NaI(Tl) crystal before the prompt cut. Since the figure shows the same one-band structure as in the plot from $\pi \to \mu \to e$ decays, the particles detected in the NaI(Tl) are likely photons.

The same selection cuts as for the 74 MeV/c data set including the prompt cut were applied to the Mylar data. The energy spectrum in the NaI(Tl) crystal is shown in figure 4.23. Only 35 events were left after the selection cuts, consequently, the Mylar data was not used for the direct analysis of the zirconium data.

4.3.12 Background Spectra

After applying all of the selection cuts described above to both of the zirconium data sets, the remaining background was studied. Figure 4.24 shows the energy-blinded time spectrum for the 72 MeV/c momentum set. It is composed of a prompt

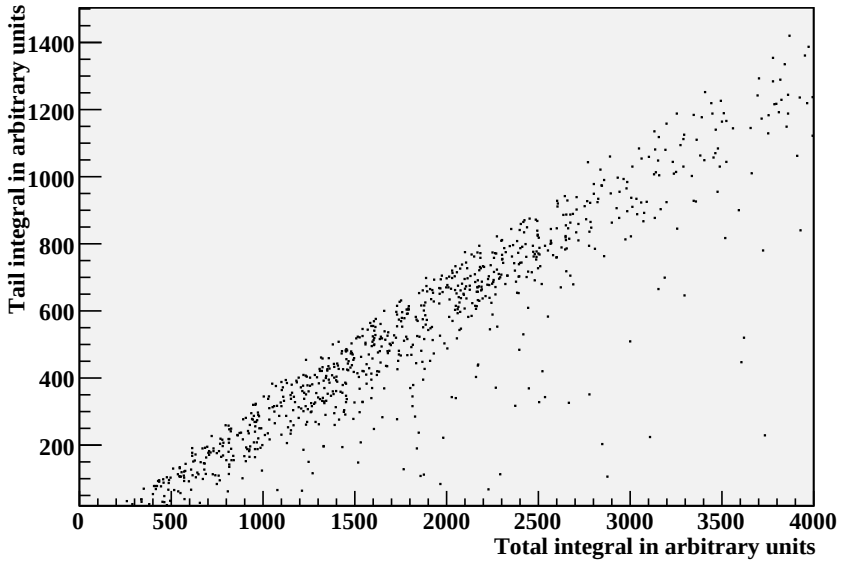

Figure 4.22: Tail versus total integral of the pulse shape in NaI(Tl) for the Mylar data before the prompt cut. Note that a different plotting style was used for this plot compared to the 72 MeV/c pulse shape plots due to the low statistics.

component, fitted by a Gaussian function in blue in the plot, and by an exponential component, fitted to an exponential function in red, with a lifetime of $\tau = 113\,\text{ns}$. This lifetime agrees well with the one measured for muon capture in zirconium ($\tau = (110 \pm 1)\,\text{ns}$ [35]), so this component most likely originates from the capture at rest process. The prompt component could be due to bremsstrahlung from muons stopping before reaching the T2 counter, as they would have been rejected by the trigger otherwise. (It was not possible to address this issue at present.) The energy-blinded and prompt-blinded energy spectra for the lower momentum case are shown in figure 4.25. There are significantly fewer background events within the signal region in the energy-blinded spectrum with the prompt cut applied. In the case of the higher momentum set, fewer muons stopped in the zirconium foil, leading to fewer background events due to the muon capture at rest. The two differently blinded energy spectra are shown in figure 4.26.

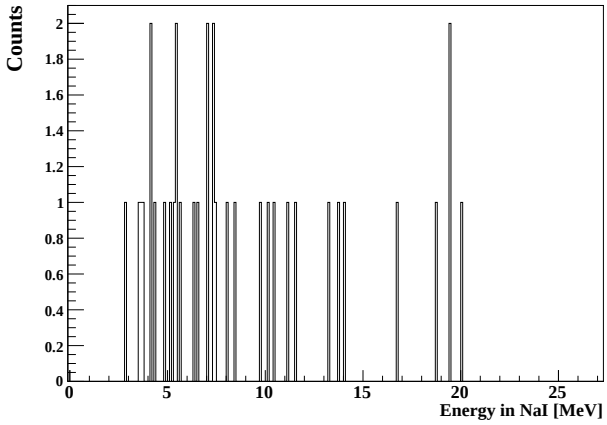

Figure 4.23: Energy spectrum in the NaI(Tl) for the Mylar data after the prompt cut.

4.4 Signal versus Background Prediction

The final step was to select the signal from within the remaining background. To do so, we developed a procedure to extract the signal peak by using the simulated signal energy spectrum, and the background spectrum from the blinded data. Combining them resulted in an energy spectrum that we expected if the signal events were observed in the data as predicted theoretically. From this combined spectrum, the signal events were then recovered and their statistical significance was assessed.

For a realistic representation of the signal, the energy spectrum from the simulation described in section 4.3.1 was used. In addition, the expected number of signal events for our experimental setup was needed. The latter was calculated from the theoretical cross section by integrating from the initial momentum of the muons entering the zirconium p_i to their momentum when exiting the foil p_f and by integrating over the whole angular range. The angular acceptance of the NaI(Tl) crystal, A, obtained from the simulation was taken into account, as well as the total number of muons entering the zirconium foil, N_μ, for each momentum set, calculated from the rate of particles passing through the counters B1 through T1 and the composition of the beam to select only muons:

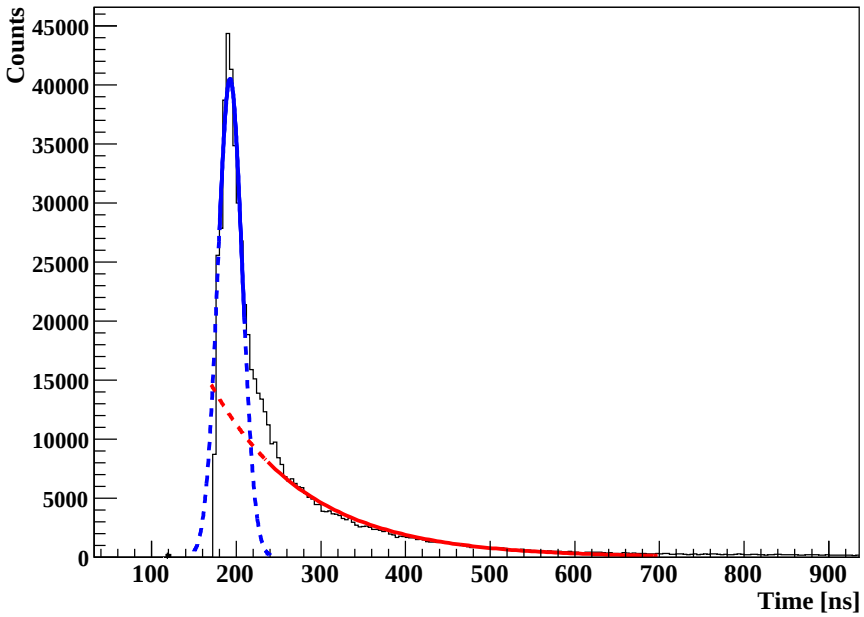

Figure 4.24: Energy-blinded time spectrum for the 72 MeV/c momentum set. A Gaussian function is fitted to the prompt region (solid blue) and an exponential to the delayed region (solid red) with a lifetime of $\tau =$ 113 ns. The dashed lines show the extensions of the fitted functions beyond the fitting range.

$$N_{signal} = A \times N_{\mu} \times \int_{p_f}^{p_i} \int \sigma \, \mathrm{d}\Omega \mathrm{d}p \tag{4.23}$$

	ARC events into the 1S state
72 MeV/c momentum set	195 events
74 MeV/c momentum set	110 events

Table 4.2: Predicted numbers of signal events in the 1S state.

The amount of signal events predicted for the two different momentum settings

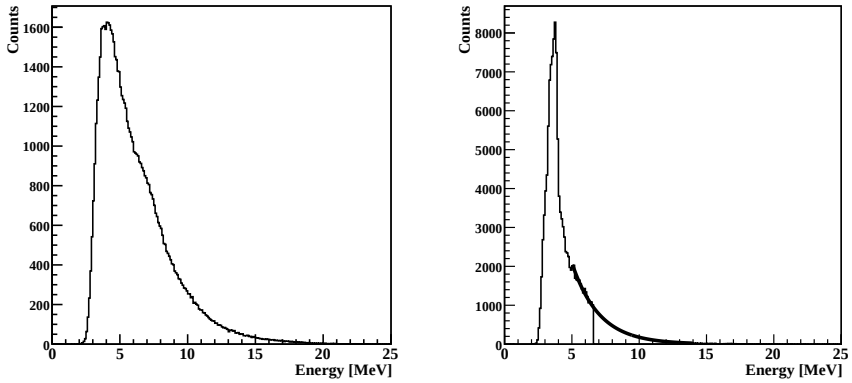

Figure 4.25: Background energy spectra for the 72 MeV/c momentum set. Left: prompt-blinded spectrum. Right: energy-blinded spectrum with an exponential fit to the blinded region.

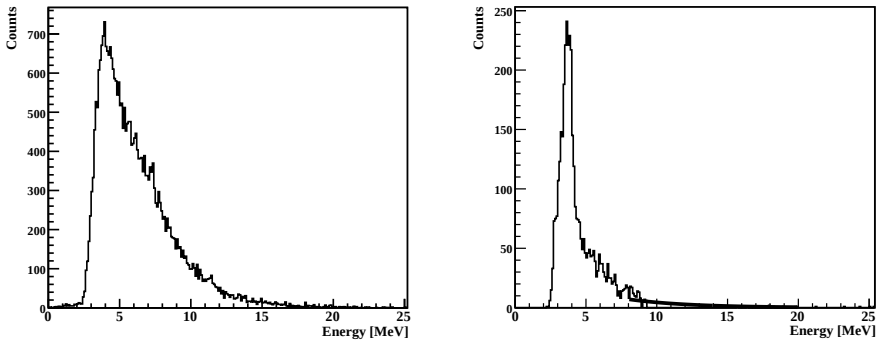

Figure 4.26: Background energy spectra for the 74 MeV/c momentum set. Left: prompt-blinded spectrum. Right: energy-blinded spectrum with an exponential fit to the blinded region.

are listed in table 4.2. Based on the amount of signal events expected within the data, a histogram was filled according to the distribution of the signal energy in the NaI(Tl). This histogram represented the signal energy with the correct distribution and statistics.

For the background spectrum, the shape of the prompt-blinded spectrum was used since it has higher statistics than the energy-blinded distribution, and the two

agree above an energy of 8 MeV, as shown in figure 4.27 for the 74 MeV/c momentum set. In the region around 4 MeV, the energy-blinded spectrum has significantly more events than the prompt-blinded spectrum, suggesting that these events originated from the prompt background component. The energy of interest for the signal, however, lies at 12.3 MeV, so the prompt-blinded shape could be used to model the background in that energy region.

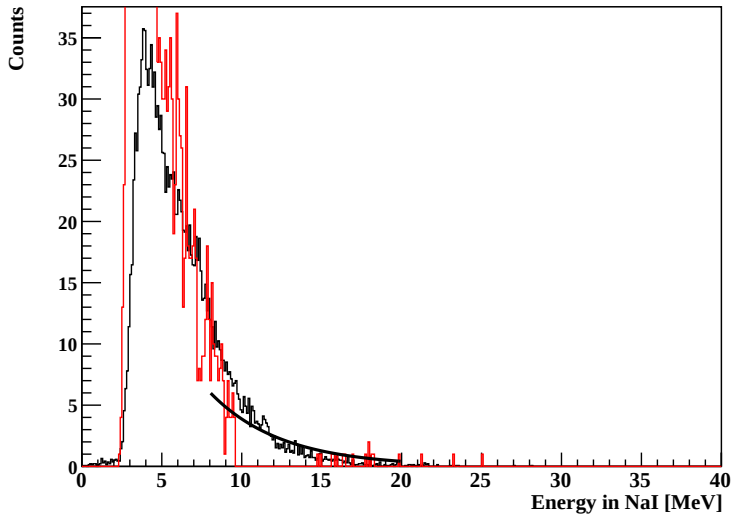

Figure 4.27: Energy-blinded spectrum (red histogram) with fit to blinded region (smooth black line) and prompt-blinded spectrum (black histogram) for 74 MeV/c data set, scaled to the energy-blinded spectrum above 8 MeV.

A histogram was filled according to the number of events in the energy-blinded spectrum above 8 MeV and the shape of the prompt-blinded spectrum to represent the background in that energy region; it is shown in the left panel of figure 4.28. By adding the signal energy distribution to this background spectrum we obtained a combined spectrum representing the data with the expected signal, shown in the middle panel of figure 4.28. Now, a second background histogram was constructed according to the prompt-blinded shape and with the statistics of the prompt-blinded spectrum, scaled down to the number of events in the energy-blinded spectrum.

This was used as background shape to subtract the background from the combined spectrum. The higher statistics were used for the filling procedure, since this spectrum will be available from the data when performing the method on the unblinded data set. For the combined spectrum, the background was filled with lower statistics as this corresponds to the expected data spectrum after all the selection cuts. The difference between the combined spectrum and the background shape, called "difference spectrum" from now on, is shown in the right panel of figure 4.28. For the extraction of the signal amount from the difference spectrum, two methods were studied:

1. The integral of the difference spectrum within one σ of the expected signal energy was calculated.

2. The difference spectrum was fitted to a Gaussian function, and its mean and integral were extracted.

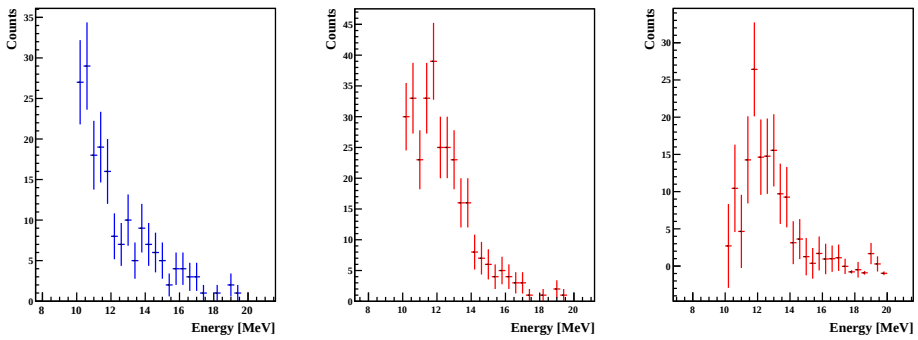

Figure 4.28: Left: constructed background spectrum. Middle: combined simulated signal and background spectrum. Right: difference between combined and background spectrum. (74 MeV/c data set)

For both of these cases, the procedure was repeated 1000 times to study the statistical effects. For the first method, the number of events in the difference spectrum within one σ of the expected signal energy is shown in the left panel of figure 4.29. Its right panel shows the number of events divided by their uncertainty, this serves as a measure for the significance of the extracted signal, i.e. a value of 5 means that the signal was extracted with a significance of 5 σ.

For the second method involving the Gaussian fit to the difference spectrum,

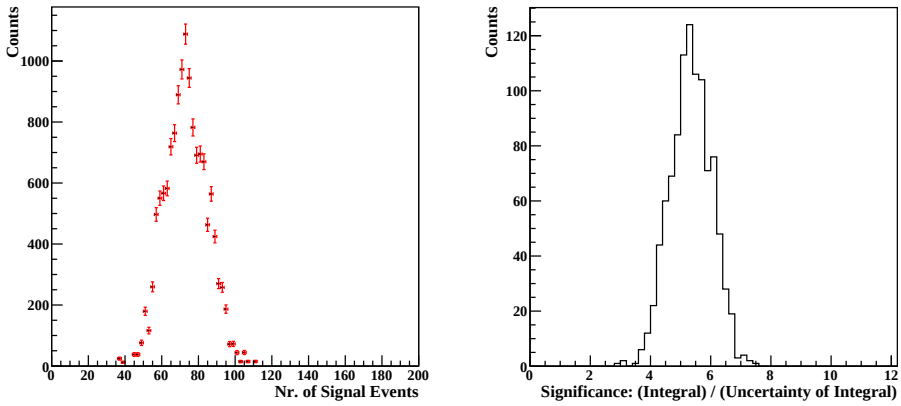

Figure 4.29: Left: integral of the difference spectrum within one σ of the expected signal. Right: significance, defined as integral / (uncertainty of integral). (74 MeV/c data set)

the integral of the Gaussian within one σ of the expected signal energy is shown in the left panel of figure 4.30. The significance for this method is defined as the amplitude of the Gaussian, divided by its uncertainty determined from the fit. This quantity is shown in the right panel of figure 4.30.

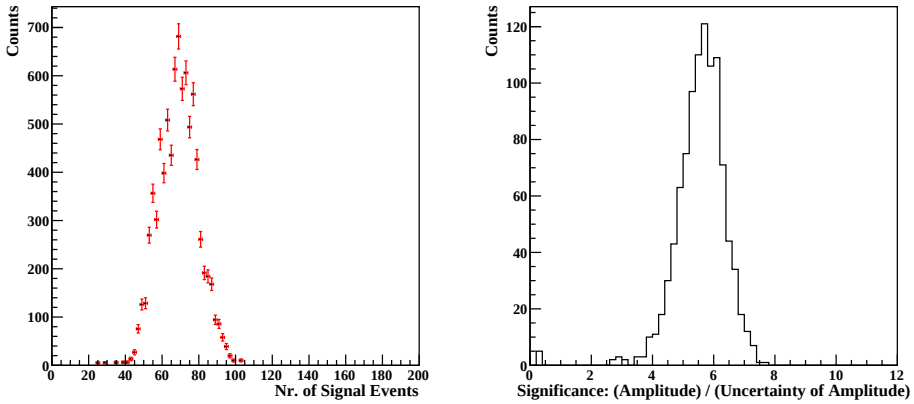

Figure 4.30: Left: integral of the Gaussian within one σ of the expected signal. Right: significance, defined as (amplitude of the Gaussian) / (uncertainty of the amplitude). (74 MeV/c data set)

When comparing figures 4.29 and 4.30, we notice that the two methods produce very similar results for the 74 MeV/c data set. With both methods, the amount of extracted signal events has a mean of 70 events, which agrees with the amount of signal events from the input spectrum within one σ around the signal energy. The significance varies between 4 and 7 σ.

For the lower momentum set, the same methods were applied to extract the signal. Figure 4.31 shows the energy-blinded spectrum together with the prompt-blinded spectrum, scaled to the number of events in the energy-blinded spectrum above 8 MeV. The two spectra differ at a higher energy more than in the 74 MeV/c momentum set, but at the signal energy of 9.3 MeV they agree sufficiently well, so the same procedure was used for the signal extraction.

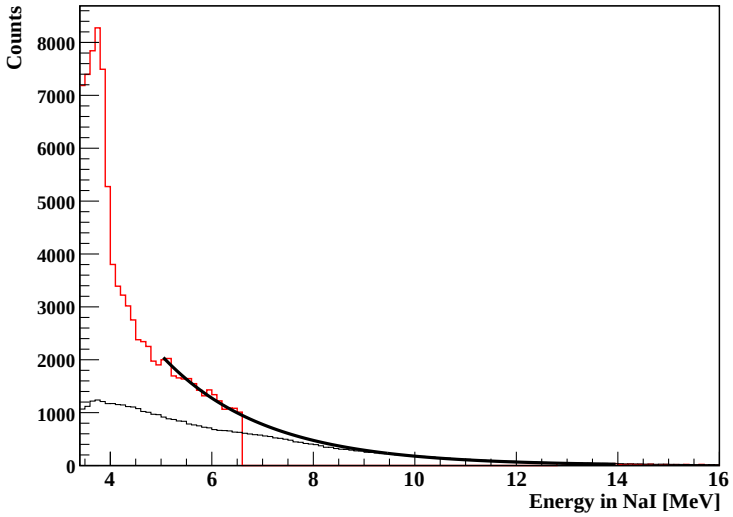

Figure 4.31: Energy-blinded spectrum (red histogram) with fit to blinded region (smooth black line) and prompt-blinded spectrum (black histogram) for 72 MeV/c data set, scaled to the energy-blinded spectrum above 8 MeV.

The results from the statistical study are shown in figure 4.32 for the integral method and in figure 4.33 for the Gaussian fit method. Using the integral method, the amount of signal is recovered with a significance of approximately one σ, vary-

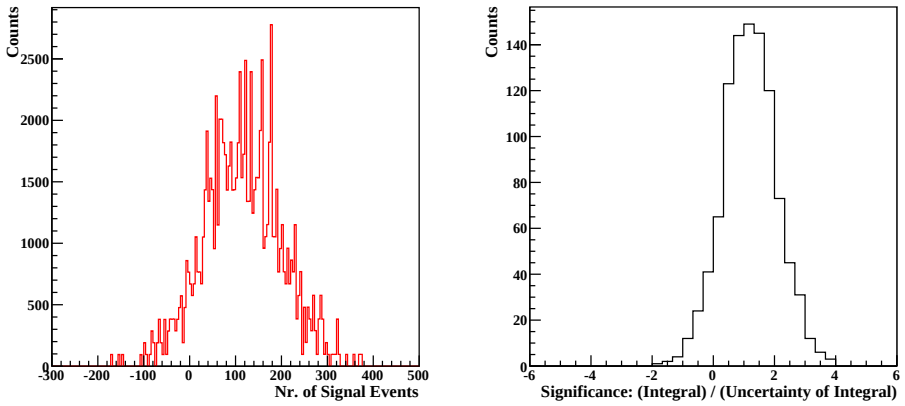

Figure 4.32: Left: integral of the difference spectrum within one σ of the expected signal. Right: significance, defined as integral / (uncertainty of integral). (72 MeV/c data set)

ing between no recovery and four σ. When the Gaussian fit is applied, the significance is zero for 42 % of the cases, meaning that the signal was not recovered. Accordingly, the amount of signal calculated for these cases is zero. Due to the high background in the 72 MeV/c momentum case, the signal can therefore only be recovered in $\sim 2/3$ of the cases. However, when the fitting procedure works, it provides additional information about the position of the peak, namely the signal energy, which is not obtained by simply integrating at the expected region as in the integral method.

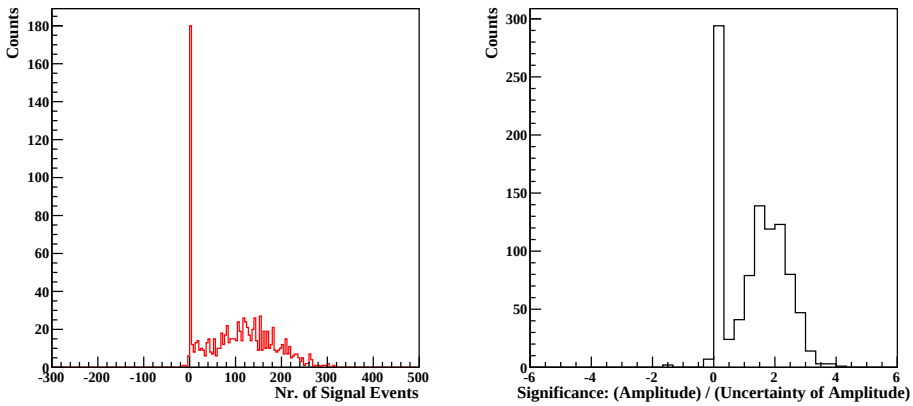

Figure 4.33: Left: integral of the Gaussian within one σ of the expected signal. Right: significance, defined as (amplitude of the Gaussian) / (uncertainty of the amplitude). (72 MeV/c data set)

Chapter 5

Conclusions

5.1 PIENU Experiment

The analysis of the PIENU data is currently underway and therefore the data is still blinded. Consequently, a final result for the branching ratio has not been determined yet. For this thesis, a lower limit was estimated for the largest systematic correction to the branching ratio due to leakage out of the calorimeters and radiative decays. It amounts to $TF = (2.24 \pm 0.07(stat) \pm 0.14(sys))\,\%$. This agrees well with the estimate from the lineshape measurement of $TF = (2.25 \pm 0.06)\,\%$. Both values provide us with an estimate of the correction, which we obtained from the data, only using the simulation for corrections that cannot be extracted from the data. This is important, since this multiplicative correction is the largest among other corrections that are applied to the branching ratio.

The largest contribution to the uncertainty of the lower limit originates mainly from the systematic uncertainty of the Bhabha correction. Since this is due to the mismatch between MC and data, there is most likely room for improvement that will decrease the systematic error on the lower limit considerably. The estimate of the MDIF fraction causes the second largest contribution to the systematic uncertainty. By studying the simultaneous fit of the energy and time spectrum of the suppressed spectrum in more detail, this can likely be reduced as well.

To reach the goal of the PIENU experiment of determining the branching ratio $R = \frac{\pi^+ \to e^+ \nu_e + \pi^+ \to e^+ \nu_e \gamma}{\pi^+ \to \mu^+ \nu_\mu + \pi^+ \to \mu^+ \nu_\mu \gamma}$ with a precision of at least 10^{-3}, the main challenge con-

stitutes in understanding all of the systematic effects and backgrounds very well to decrease the systematic uncertainty. The work for this thesis contributed to the understanding of the largest systematic effect.

5.2 Muon Capture Experiment

The experiment described in the second part of this thesis is the first attempt of measuring the direct radiative capture of muons into the 1S state of zirconium. The background process due to muon capture at rest was sufficiently suppressed in the higher momentum data set by achieving a time resolution of 4 ns in the NaI(Tl) crystal and by applying a pulse shape discrimination method successfully. With a simulation of the energy spectrum combining signal and background, the recovery of the signal was shown to be possible with a significance of five σ for the 74 MeV/c momentum set if the signal has the characteristics as predicted by the theory.

In the lower momentum set with a higher level of background, the signal could only be recovered in 2/3 of the cases. When unblinding the data set, the results for the 72 MeV/c data set should be compared to the 74 MeV/c data set and studied for consistency. Consequently, the data was not unblinded yet, and further attempts of decreasing the background and increasing the signal significance are currently underway. One possibility of identifying stopping muons which contribute to the background is to study the energy deposit in the T1 counter, which is located directly in front of the zirconium foil and compare it to the total energy loss in the detectors upstream of the foil. The same study can be done with the GEANT4 simulation, where the fact whether or not a muon stops in the zirconium is known. Since slow muons have a higher dE/dx in the T1 counter than those with higher kinetic energy, the ones stopping in the zirconium could be identified. Consequently, a further cut decreasing the amount of stopped muons in the zirconium could be applied to suppress more background events.

After unblinding the data, the same procedure for signal recovery as explained for the simulated signal in section 4.4 will be applied. The only difference will be to use the unblinded data spectrum instead of the constructed combined spectrum. One possible scenario is to extract a signal with exactly the same properties as

predicted by the theory. However, is also possible that no signal is observed or it could have a different magnitude or be extracted at a different energy. In those cases, the spectrum can be probed for a signal at different energies or an upper limit on the cross section for the direct radiative capture into the 1S state of zirconium can be set.

Whether the predicted cross section is confirmed by this experiment, or an upper limit is set on the cross section of the ARC process, this study will provide important information for future experiments in the field. It will provide crucial knowledge on the cross section of the direct radiative capture for the case that the experiment suggested in reference [13] is carried out in total to probe for a parity-violating process. If a signal is extracted, this would be the first measurement of a muon capture directly into the 1S state. In case a limit is set, essential information for future attempts of measuring the direct radiative capture is provided by this experiment.

Bibliography

[1] C. Malbrunot, Ph.D. thesis, University of British Columbia (2012). → pages

[2] T. Sullivan, Tech. Rep., PIENU collaboration, TRIUMF (April 2013). → pages

[3] V. Cirigliano and I. Rosell, Phys. Rev. Lett. **99**, 231801 (2007), URL http://link.aps.org/doi/10.1103/PhysRevLett.99.231801. → pages

[4] J. Beringer et al. (Particle Data Group), Phys. Rev. D **86**, 010001 (2012), URL http://link.aps.org/doi/10.1103/PhysRevD.86.010001. → pages

[5] G. Aad et al. (ATLAS Collaboration), Phys.Lett. **B716**, 1 (2012), 1207.7214. → pages

[6] Y. Fukuda et al. (Super-Kamiokande Collaboration), Phys.Rev.Lett. **81**, 1562 (1998), hep-ex/9807003. → pages

[7] V. Rubin, N. Thonnard, and J. Ford, W.K., Astrophys.J. **238**, 471 (1980). → pages

[8] N. Okabe, G. P. Smith, K. Umetsu, M. Takada, and T. Futamase, The Astrophysical Journal Letters **769**, L35 (2013), URL http://stacks.iop.org/2041-8205/769/i=2/a=L35. → pages

[9] P. Ade et al. (Planck Collaboration) (2013), 1303.5077. → pages

[10] M. Aoki, M. Blecher, D. A. Bryman, S. Chen, M. Ding, L. Doria, P. Gumplinger, C. Hurst, A. Hussein, Y. Igarashi, et al. (PIENU Collaboration), Phys. Rev. D **84**, 052002 (2011), URL http://link.aps.org/doi/10.1103/PhysRevD.84.052002. → pages

[11] G. Bennett et al. (Muon G-2 Collaboration), Phys.Rev. **D73**, 072003 (2006), hep-ex/0602035. → pages

[12] R. Pohl et al., Nature Publishing Group, a division of Macmillan Publishers Limited. All Rights Reserved. **0028-0836** (2010), http://www.nature.com/nature/journal/v466/n7303/full/nature09250.html. → pages

[13] D. McKeen and M. Pospelov, Phys. Rev. Lett. **108**, 263401 (2012), URL http://link.aps.org/doi/10.1103/PhysRevLett.108.263401. → pages

[14] A. Aguilar-Arevalo, M. Blecher, D. Bryman, J. Comfort, J. Doornbos, et al., Nucl.Instrum.Meth. **A609**, 102 (2009), 1001.3121. → pages

[15] A. Aguilar-Arevalo et al. (PIENU Collaboration), *The pienu detector* (to be pub. (2014)). → pages

[16] S. Ritt and P. A. Amaudruz, *The midas data acquisition system* (Available from: midas@triumf.ca). → pages

[17] L. Doria, Tech. Rep., PIENU collaboration, TRIUMF (July 2011). → pages

[18] C. Malbrunot and M. Aoki, Tech. Rep., PIENU collaboration, TRIUMF (August 2010). → pages

[19] D. Protopopescu, D. Britton, and I. Skillicorn, Tech. Rep., PIENU collaboration, TRIUMF (October 2013). → pages

[20] D. vom Bruch, Tech. Rep., PIENU collaboration, TRIUMF (November 2013). → pages

[21] A. Aguilar-Arevalo, M. Aoki, M. Blecher, D. Bryman, L. Doria, et al., Nucl.Instrum.Meth. **A621**, 188 (2010), 1003.2235. → pages

[22] S. Cuen-Rochin, Tech. Rep., PIENU collaboration, TRIUMF (May 2013). → pages

[23] T. Numao, Tech. Rep., PIENU collaboration, TRIUMF (March 2013). → pages

[24] P. J. Mohr, B. N. Taylor, and D. B. Newell, Rev. Mod. Phys. **80**, 633 (2008), URL http://link.aps.org/doi/10.1103/RevModPhys.80.633. → pages

[25] J. Beringer et al. (Particle Data Group), PR **D86** (2012), URL http://pdg.lbl.gov. → pages

[26] B. Batell, D. McKeen, and M. Pospelov, Phys. Rev. Lett. **107**, 011803 (2011), URL http://link.aps.org/doi/10.1103/PhysRevLett.107.011803. → pages

[27] L. D. Landau and E. M. Lifshitz, *Quantum Electrodynamics* (Pergamon Press, 1971). → pages

[28] J. Missimer and L. Simons, Phys. Rept. **118**, 179 (1985). → pages

[29] H. A. Bethe and E. E. Salpeter, *Quantum Mechanics of One- and Two-Electron Atoms* (Springer Verlag, 1957). → pages

[30] O. B. van Dyck, E. W. Hoffman, R. J. Macek, G. Sanders, R. D. Werbeck, and J. K. Black, IEEE Transactions on Nuclear Science **NS-26** (1979). → pages

[31] M. Pospelov and A. Fradette, Private Communication (2013). → pages

[32] T. Q. Phan, P. Bergem, A. Rüetschi, L. A. Schaller, and L. Schellenberg, Phys. Rev. C **32**, 609 (1985), URL http://link.aps.org/doi/10.1103/PhysRevC.32.609. → pages

[33] P. Kammel, Y. Kuno, et al., Research Proposal (2012). → pages

[34] M. E. Plett and S. E. Sobottka, Phys. Rev. C **3**, 1003 (1971), URL http://link.aps.org/doi/10.1103/PhysRevC.3.1003. → pages

[35] T. Suzuki, D. F. Measday, and J. P. Roalsvig, Phys. Rev. C **35**, 2212 (1987), URL http://link.aps.org/doi/10.1103/PhysRevC.35.2212. → pages

[36] J. Beringer et al., Phys. Rev. D **86** (2012). → pages

[37] J. Birks, *The Theory and Practive of Scintillation Counting* (Pergamon Press, 1964). → pages

[38] P. Doll et al., Nuclear Instruments and Methods in Physics Research **A285**, 464 (1989). → pages

[39] G. Share, J. Kurfess, and R. Theus, Nuclear Instruments and Methods **148**, 531 (1978). → pages